Fabrication, Analysis, and Modelling of SS316L & IN625 FGMs and Alloys by Twin Wire Arc Additive Manufacturing

M.Tech. Thesis

By

ATLURI BHARATH KUMAR

(2102103002)

DEPARTMENT OF MECHANICAL ENGINEERING

INDIAN INSTITUTE OF TECHNOLOGY INDORE

MAY 2023

Fabrication, Analysis, and Modelling of SS316l & IN625 FGMs and Alloys by Twin Wire Arc Additive Manufacturing

A THESIS

Submitted in partial fulfillment of the requirements for the award of the degree
of
Master of Technology

by

ATLURI BHARATH KUMAR
(2102103002)

DEPARTMENT OF MECHANICAL ENGINEERING
INDIAN INSTITUTE OF TECHNOLOGY INDORE
May 2023

INDIAN INSTITUTE OF TECHNOLOGY INDORE

CANDIDATE'S DECLARATION

I hereby certify that the work which is being presented in the thesis entitled **Fabrication, analysis, and modelling of SS316l & IN625 FGMs and Alloys by Twin Wire Arc Additive Manufacturing** in the partial fulfillment of the requirements for the award of the degree of **MASTER OF TECHNOLOGY** and submitted in the **DEPARTMENT OF MECHANICAL ENGINEERING, Indian Institute of Technology Indore**, is an authentic record of my own work carried out during the time period from June 2021 to May 2023 under the supervision of **Dr. Yuvraj Kumar Madhukar**, Assistant Professor, Department of Mechanical Engineering, Indian Institute of Technology, Indore.

The matter presented in this thesis has not been submitted by me for the award of any other degree of this or any other institute.

A Bharath
05/06/2023

Atluri Bharath Kumar
(2102103002)

This is to certify that the above statement made by the candidate is correct to the best of our knowledge.

Dr. Yuvraj Kumar Madhukar 05/06/2023

(Dr. Yuvraj Kumar Madhukar)

Mr. Atluri Bharath Kumar has successfully given his M.Tech. Oral Examination held on **May 26, 2023**.

Dr. Yuvraj Kumar Madhukar 05/06/2023

Signature(s) of Supervisor(s) of M.Tech. thesis
Date:

Satyanarayan

Convener, DPGC
Date: 05/06/2023

Signature of PSPC Member #1
Dr. Ashish Rajak
Date: 05/06/2023

Abhijit Ghosh

Signature of PSPC Member #2
Dr. Abhijit Ghosh
Date: 05/06/2023

ACKNOWLEDGEMENTS

My deep gratitude goes first to my supervisor, **Dr. Yuvraj Kumar Madhukar**, who expertly guided me throughout my two years of Master of Technology. I was fortunate to have advisors who offered me the constant motivation and productive support that preceded this work to attain this form. I would also like to thank my PSPC members, Dr. Ashish Rajak and Dr. Abhijit Ghosh for their continuous inputs for the advancement of this project. A very special thanks to Mr. Anas Ullah Khan (Ph.D. scholar), and Mr. Shubham Sadhya (Ph.D scholar) for their moral support and supportive environment for the completion of the project. Thanks also goes to my batch-mates for their moral support throughout this journey. I am also thankful to Metallography Laboratory, Laser Material Processing, and Central Workshop at IIT Indore. I cannot end my words without expressing my heartfelt thanks and admiration for my dear parents' blessings and efforts to maintain my morale throughout my project. I would like to offer my heartfelt gratitude to everyone who has assisted me in any way, whether directly or indirectly, during this project.

With Regards,
Atluri Bharath Kumar

DEDICATED TO

My beloved Parents and sisters

for their unwavering support

throughout the journey

ABSTRACT

The research paper focused on the fabrication of functionally graded materials (FGMs) and alloys using the TIG-based wire arc additive manufacturing (WAAM-TIG) process. The study explores two types of functionally graded materials (FGMs) i.e., continuous (CG-FGM) and sandwich structures (SW-FGMs) with varying gradients. By precisely controlling the weight percentage of SS316L and IN625 materials using individual wire feeding systems, defect-free depositions are achieved through the optimization of process parameters. Energy dispersive X-ray spectroscopy (EDS) analysis reveals a gradual variation in the distribution of Ni and Fe elements in CG-FGMs, while alternating peaks are observed in SW-FGMs. Microstructure analysis shows a smooth transition from equiaxed to columnar dendrites in CG-FGMs, while SW-FGMs exhibit a heterogeneous behavior. Hardness measurements indicate a steady increase in CG-FGMs and a wavy pattern in SW-FGMs. X-ray diffraction (XRD) analysis confirms the formation of the desired austenitic phase, with peak height variations correlating to changes in microstructure and hardness. The specific wear rate decreases with increasing Ni content in CG-FGMs, while in SW-FGMs, it shows a strong dependency on the adopted design. In statistical study, response surface design analysis was conducted using central composite design (CCD). Regression models were developed to evaluate factors' effects on responses such as hardness, fracture toughness, scratch hardness, specific wear rate, and coefficient of friction (COF) that exhibited the R^2 values ranging between 0.65 to 0.9. Composition is found to be the main factor influencing the mechanical properties, while current and speed affect bead geometry. Quadratic models were determined to be the most suitable for most responses. The optimal conditions for maximizing hardness and fracture toughness and minimizing wear rate were identified as a composition of 3 (3:1), current of 205 A, and voltage of 200 mm/min. The predicted values for the selected parameters were also presented, along with an overall composite desirability value of 0.63.

Keywords: Additive manufacturing, functionally graded material, directed energy deposition, design of experiments, CCD, SS316L, IN625.

Table of Contents

LIST OF FIGURES

LIST OF TABLES

NOMENCLATURE

C	Alloy Composition
I	Arc Current
S	Travel speed
COF	Coefficient of Friction
WRR	Specific Wear Rate
CG-FGM	Continuous gradient FGM
SW-FGM	Sandwich structured FGM
ABAB	Single set sandwich structured FGM
AABB	Double set sandwich structured FGM
AAABBB	Triple layered sandwich structured FGM

ACRONYMS

FGMs	Functionally Graded Materials
AM	Additive Manufacturing
WFR	Wire Feed Rate
WAAM	Wire Arc Additive Manufacturing
TIG	Tungsten Inert Gas
GTAW	Gas Tungsten Arc Welding
GMAW	Gas Metal Arc Welding
DED	Directed Energy Deposition
LENS	Laser Engineered Net Shaping
DMLS	Direct Metal Laser Sintering
PBF	Powder Bed Fusion
LMD	Laser metal deposition
EDS	Energy Dispersive Spectroscopy
SEM	Scanning Electron Microscope
CMT	Cold Metal Transfer

Chapter 1 Introduction

1.1. Overview

Additive manufacturing, also known as 3D printing, is poised to revolutionize the manufacturing industry. With its ability to print parts layer by layer, further creating complex and intricate parts quickly and easily, it is transforming the way products are designed, developed, and produced. It enables engineers to design and create parts that were once impossible to produce using traditional methods, resulting in improved efficiency, reduced costs, and faster time-to-market. Additive manufacturing also offers the ability to use new materials, such as advanced composites and alloys, which have superior strength-to-weight ratios and other unique properties. Functionally graded materials, a class of advanced materials that have varying properties and characteristics across their structure. This enables them to perform different functions in different areas of a component. By blending different materials together in precise ratios, manufacturers can create materials that are stronger, more durable, and more adaptable than traditional materials. Additive manufacturing and functionally graded materials (FGMs) are two innovative technologies that are changing the face of the manufacturing industry. When combined, they offer even greater potential to revolutionize the industry. For example, FGMs can be printed using various additive manufacturing techniques, enabling the creation of parts with intricate internal structures and varying material properties. This means that aerospace and automotive engineers can design and produce parts that are not only lighter and more efficient, but also stronger, more durable, and more adaptable to different conditions.

1.2. Functionally graded materials

The fabrication of multicomponent functionally graded material (FGM) has received a significant upswing in recent years with the advancement in layer-by-layer deposition/additive manufacturing processes. The localisation of stress eccentric fields and extreme temperatures at different regions of

mechanical component and tools is observed frequently [1]. For example, the critical parts in a nuclear reactor, and air crafts at high altitude should be able to resist significant temperature fluctuations. A solution could be to use materials such as composites with localised mechanical properties. However, composites cannot serve these functionalities for a long period [2] due to the possibility of delamination failure [3]. These stress concentrations and thermal creep problems can be controlled if the variation in localised properties is gradual or as engineered. To address this limitation, Naotoke designed an advanced family of composite structures known as functionally graded materials (FGMs) based on the inference of naturally occurring materials (teeth, wood and bone). These natural materials are generally composed of graded regions and thus giving advanced properties than those of individual composite structures.

FGMs can reduce the cost and weight of produced parts while enhancing the yield and fracture thresholds. In few applications, FGM also helps in overcoming the tribological properties such as corrosion and abrasive wear [4]. It was conceptualised for the first time at a research lab in Japan in 1984 for the aerospace research project [5]. FGMs can also be designed to vary the materials gradually over volume or with presence of controllable fusion zone even for step change. Fig. 1b illustrates the stress fields at the interface in directly joining and gradient joining of SS304l / Inconel 625. Moreover, Functional Gradient Materials (FGMs) are being used in various industries due to their unique properties as shown in Fig. 1a. They are used in aerospace, military, energy, manufacturing, medicine, and other industries. In the aerospace industry, FGMs are used to manufacture high-performance equipment and structures like rocket engine components, radomes spacecraft truss structure, heat exchange panels, reflectors, solar panels, camera housing, turbine wheels, nose caps, the leading edge of missiles, and space shuttles. FGMs are used in energy devices such as piezoelectric FGMs for ultrasonic transducers, actuators, damping materials, energy absorption, energy harvesting, thermoelectric converters for energy conversion, solar panels, solar cells, fuel cells, turbine blade coatings, and the graded electrode for the

production of solid oxide fuels cells. In the military industry, FGMs are used to manufacture equipment and structures for combat applications, and in medicine, they are used in implants, prosthetics, and other medical equipment. FGMs are also used in manufacturing processes like cutting tools, coatings, and surface treatment materials. The use of FGMs has revolutionized various industries by improving the efficiency and quality of the final products while reducing costs.

Fig. 1.1 a) The application fields of FGMs. b) Finite element analysis of a gradient transition from 304L stainless steel to Inconel 625 (left) compared to a friction-welded joint of the same materials (right) for an automobile valve stem at operating temperature 1000 K [6].

The different design characteristics of FGM have been reported by various researchers over the period. Functionally graded materials (FGMs) can be classified into three conventional classifications. The first classification is based on the state of FGM processing, which can be solid-state processes, liquid-state processes, or deposition processes. The second classification is based on the FGM structure, which can be either continuous or discontinuous graded material. Continuous and discontinuous graded materials can further be classified based on composition gradient, orientation gradient, and fraction gradient. The third classification is based on the type of FGM gradient, which can be composition, microstructure, or porosity. Lastly, FGMs can be classified based on their scale and dimensions, such as thin FGMs, which are manufactured by physical vapor deposition, chemical vapor deposition, thermal spray deposition, or self-propagating high-temperature synthesis techniques like laser cladding. The classification of FGMs is important to determine the appropriate manufacturing process and

understand the characteristics of the final product. FGMs in this research were classified based on the variation in chemical composition such as continuous gradient (CG-FGM) and sandwich type (SW-FGM) for stepped gradient [7]. Gradient materials can be categorized into two groups based on their size and structure. In terms of size, gradients can either be thin-section, resembling surface coatings, or bulky, which require distinct processing techniques. Based on structure, they can be classified as continuous or discontinuous. Discontinuous gradient materials (Fig. 2a) exhibit a stepwise change in chemical composition or microstructure, and the interface is usually visible. Conversely, in continuous gradient materials (Fig. 2b), the chemical composition or microstructure changes continuously, resulting in a graded structure without a distinct boundary. Fig. 2c-h illustrates the general schemes of gradient materials with varying structure types [18]. The selection of production method plays a vital role in achieving high quality and performance of FGM based on economic and environmental considerations [8].

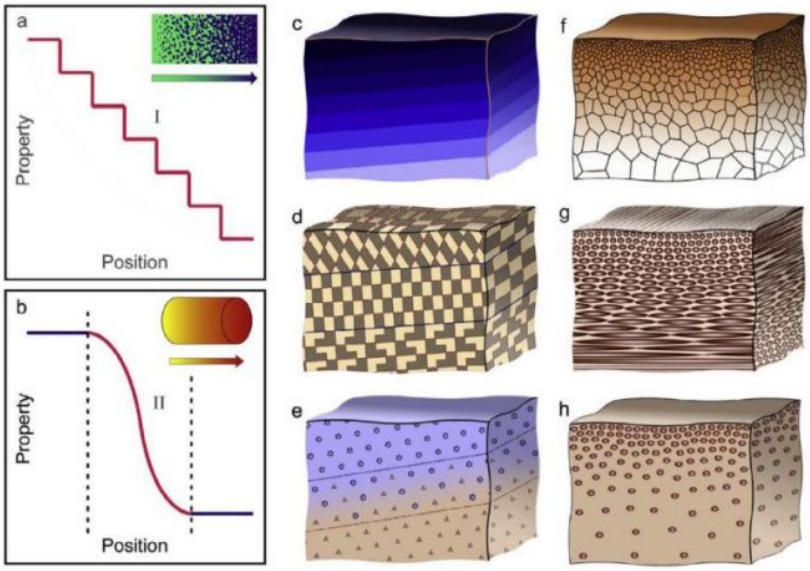

Fig. 1. 2 Functionally graded materials with different forms of gradient [45]. (a) Discrete/discontinuous FGMs with interface. (b) Continuous FGMs with no interface. (c), (f) Composition gradient. (d), (g) Orientation gradient. (e), (h) Fraction gradient. [6]

1.3. Production Methods of FGM

Fusion welding, powder metallurgy [9], centrifugal casting, thermal spraying (CVD, PVD), and additive manufacturing techniques (SLS, SLM, LENS) [6]

are few of the processes that could be executed to develop FGM with finite gradient.

1.3.1. Conventional Methods

Conventional manufacturing methods for producing functionally graded materials (FGMs) include chemical/physical vapor deposition techniques, thermal spraying, powder metallurgy, spark plasma sintering, centrifugal casting, and self-propagating high-temperature synthesis.

1. ***CVD/PVD techniques:*** Chemical and physical vapor deposition techniques involve the deposition of thin films on a substrate. The precursor material is vaporized and transported to the substrate, where it reacts to form a solid film. This method is capable of producing high-quality coatings with precise thickness control, but it is limited by the size of the substrate and the difficulty of scaling up the process. Thermal spraying involves the spraying of molten or semi-molten material onto a substrate. The material is heated to its melting point and sprayed onto the substrate, where it solidifies to form a coating. This method is commonly used for producing thermal barrier coatings and wear-resistant coatings, but it has limitations in terms of the thickness and quality of the coatings that can be produced.

2. ***Powder metallurgy:*** Powder metallurgy involves the consolidation of powders into a solid material. The powders are mixed together and pressed into a compact, which is then sintered to form a solid material. This method is commonly used for producing high-strength materials with controlled microstructures, but it has limitations in terms of the complexity of the shapes that can be produced.

3. ***Centrifugal casting****:* Centrifugal casting involves the pouring of molten metal into a rotating mold. The centrifugal force generated by the rotation of the mold causes the molten metal to distribute itself evenly along the length of the mold, producing a graded structure. This method is

commonly used for producing cylindrical components with graded properties, but it is limited by the size of the mold and the difficulty of controlling the microstructure.

4. ***Spark plasma sintering:*** It involves the consolidation of powders by the application of high current and pressure. The powders are placed in a die and heated by the passage of a high-current pulse through the die. The resulting material has a fine-grained microstructure and can be produced in complex shapes, but it is limited by the size of the die and the cost of the equipment.

5. ***Self-propagating high-temperature synthesis*** involves the exothermic reaction between two or more powders to form a solid material. The reaction is initiated by heating the powders to their ignition temperature, and the resulting product is a solid material with a fine-grained microstructure. This method is commonly used for producing ceramics and intermetallic, but it has limitations in terms of the types of materials that can be synthesized.

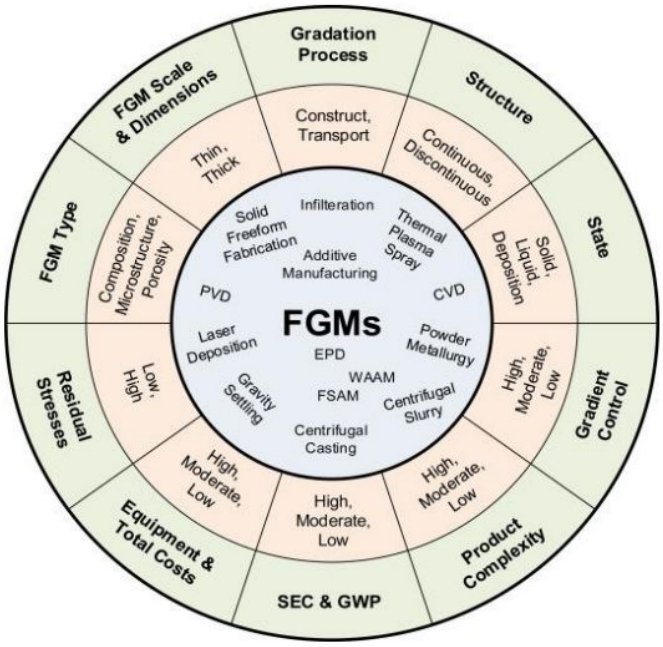

Fig. 1. 3. Classification of Conventional manufacturing methods for Functionally graded materials [11].

However, these conventional manufacturing methods have limitations in terms of the size and complexity of the parts that can be produced, as well as the energy consumption and environmental pollution associated with their use. In recent years, additive manufacturing (AM) technologies have emerged as an alternative method for producing FGMs.

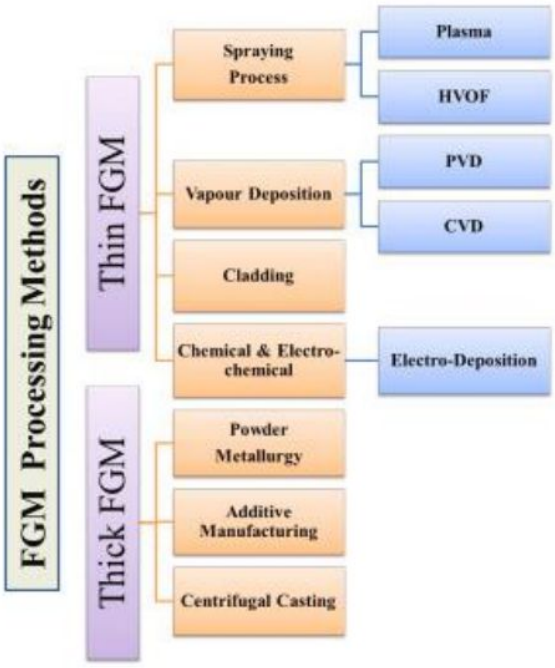

Fig. 1.4 Manufacturing methods classification based on the FGM geometry fabrication.

1.3.2. Additive Manufacturing (AM) Methods

1. Binder jet AM method

Binder jet 3D printing, a type of additive manufacturing (AM), involves the deposition of a liquid binding agent onto a powder bed of different materials, such as metals, ceramics, or composites, to selectively bind particles and form a green part. Subsequently, the green part is sintered to remove the binding agent and densify the material. The process allows for the production of functionally graded materials (FGMs), which are characterized by gradual transitions in composition, microstructure, and properties across the part. By controlling the type, amount, and distribution of the powders and binders, as

well as the printing parameters, such as layer thickness and orientation, binder jet AM can tailor the FGMs to meet specific requirements, such as mechanical strength, thermal conductivity, wear resistance, or biocompatibility, for various applications, such as aerospace, medical, or energy.

2. Photopolymerization Vat method

Photopolymerization Vat method is an additive manufacturing process that uses a vat of liquid photopolymer resin and a light source to selectively cure the resin into a solid object layer by layer. The process begins with a digital model that is sliced into multiple thin layers. The first layer is then projected onto the surface of the liquid resin, and the UV light source selectively cures the resin where the pattern is projected. The build platform then moves down to allow the next layer to be projected and cured onto the previous layer. This process is repeated until the entire object is built. To create FGM, multiple resins with varying properties are used, and the printing process can switch between them to create gradients between different materials. This method offers high accuracy, fine details, and the ability to produce complex geometries, making it suitable for manufacturing FGM with precise material properties.

3. Material Extrusion (ME)

Material Extrusion (ME) is a 3D printing method that is commonly used for manufacturing FGM. In this process, a thermoplastic filament is fed through a heated extruder and deposited layer by layer to form the final part. The extruder melts the filament and extrudes it through a nozzle to create a continuous stream of molten material. The nozzle is guided by a computer-controlled system that follows a pre-determined path to create the desired shape. The part is built up layer by layer until the final shape is achieved. The temperature of the extruder and the speed at which the filament is deposited can be adjusted to control the properties of the final part. ME is a versatile and relatively inexpensive process, making it a popular choice for

manufacturing FGM. However, the process does have limitations in terms of the resolution and surface finish that can be achieved.

4. Sheet Lamination

Sheet Lamination is a type of Additive Manufacturing (AM) process that involves the layer-by-layer addition of material using a sheet or a ribbon. In this process, a thin sheet or ribbon of material, such as paper, metal, or plastic, is cut into the desired shape using a laser or a knife, and then bonded to the previous layer using heat, pressure, or an adhesive. The process is repeated until the final object is produced. The sheet lamination process is generally less expensive than other AM methods because it uses less material and requires less complex equipment. However, the quality of the final product can be limited by the thickness of the sheet or ribbon used, which can affect the resolution and surface finish. The method is commonly used in the manufacture of functional prototypes, architectural models, and dental models, among other applications.

5. Material Jetting

Material Jetting (MJ) is an additive manufacturing process used for the production of FGM. This process involves the deposition of droplets of liquid photopolymer or wax onto a build platform using a print head. The print head is computer-controlled and dispenses the material through small nozzles, layer by layer, to create a three-dimensional object. The material is solidified or cured by UV light, which is projected onto the droplets as they are deposited, allowing them to harden and bond to each other. Multiple print heads can be used to deposit different materials or colors simultaneously, enabling the production of FGM. MJ can produce complex geometries with high accuracy and resolution, making it a suitable method for manufacturing FGM with intricate designs. However, the process is limited by the range of materials that can be jetted and the size of the build platform.

6. Powder bed fusion

Powder Bed Fusion (PBF) is a class of additive manufacturing methods that involve melting or sintering successive layers of powdered material to create a solid object. There are two main types of PBF methods used for FGM manufacturing: Selective Laser Sintering (SLS) and Selective Laser Melting (SLM). In SLS, a laser is used to selectively heat and fuse the powder particles together, layer by layer, to form the desired object. In contrast, SLM uses a laser to completely melt the powder particles, resulting in a fully dense part with no residual porosity. There is also a variation of SLM called Electron Beam Melting (EBM) that uses an electron beam instead of a laser to melt the powder particles. EBM is particularly useful for producing parts with complex geometries or internal features. Overall, PBF methods are well-suited for FGM manufacturing due to their ability to produce fully dense parts with excellent mechanical properties. However, they can be more expensive and time-consuming than other AM methods, and may require additional post-processing steps to achieve the desired surface finish.

7. Directed Energy Deposition

Directed Energy Deposition (DED) is an additive manufacturing technique used to produce FGM by melting and depositing materials layer by layer. There are two main types of DED: blown powder deposition and wire feedstock deposition. Blown powder deposition involves using a high-power laser or electron beam to melt and fuse powder particles, while wire feedstock deposition involves melting and fusing wire feedstock using a laser or electron beam.

Blown powder deposition can further be divided into two subtypes: laser blown powder deposition and electron beam blown powder deposition. Similarly, wire feedstock deposition can be further classified into laser, GTAW, GMAW and electron beam wire feedstock deposition. In both types of DED, the material is melted and deposited in a controlled manner, allowing for the creation of complex geometries and the production of multi-

material FGMs. The deposited material solidifies quickly, resulting in a strong and durable end product.

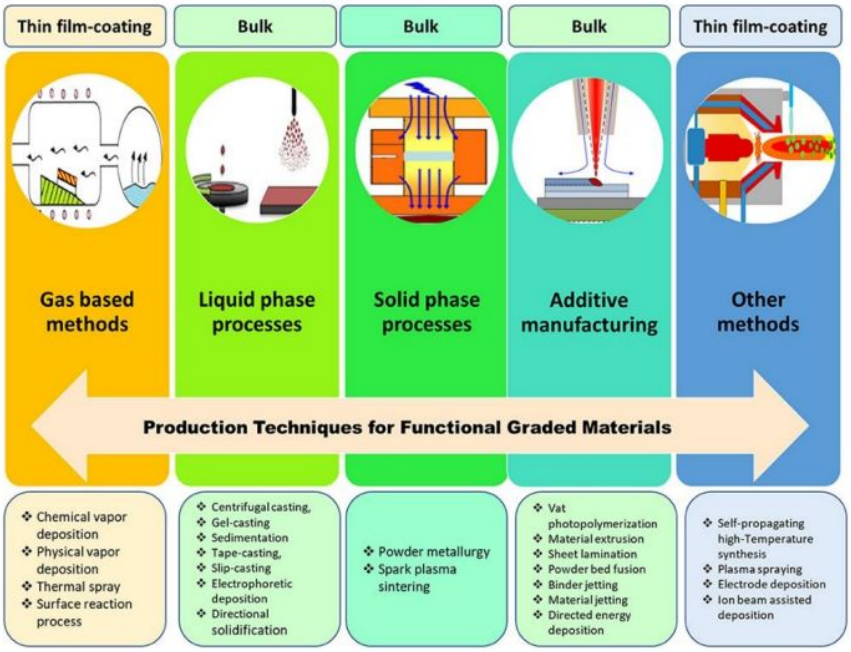

Fig. 1. 5 Classification of production techniques for FGM fabrication.

1.4. Wire Arc Additive Manufacturing (WAAM)

Wire feedstock Directed Energy Deposition (DED) deposition methods such as arc, laser, and electron beam are more suited for Functionally Graded Materials (FGM) manufacturing due to several technical advantages over other AM and conventional techniques. Firstly, wire feedstock allows for efficient material utilization and deposition rates, reducing material wastage and production time. Secondly, the ability to use multiple wire feedstocks, including metals and alloys, allows for precise control over material composition, which is crucial in FGM production. Additionally, the high-energy density of arc, laser, and electron beam processes enables the creation of complex geometries with high accuracy, further enhancing the manufacturing of FGMs. Lastly, these methods can operate in both vacuum and atmospheric conditions, increasing flexibility and applicability. Overall, wire feedstock DED deposition methods provide an efficient, precise, and flexible approach to FGM manufacturing, making them a preferred choice over other conventional techniques.

TIG-based wire arc additive manufacturing (WAAM) is considered one of the best options for producing large metal components with high accuracy and surface quality. This is because TIG welding offers a high degree of control over the heat input, which can help prevent thermal distortion and residual stresses that often arise in other AM and conventional methods. Additionally, TIG-based WAAM can be used with a variety of materials, including aluminum, nickel super alloys, titanium, and steel, and can produce near-net shape parts with minimal waste. It also provides the ability to adjust the deposition rate and layer thickness, enabling the fabrication of components with varying material properties. Overall, TIG-based WAAM offers a cost-effective and efficient solution for producing complex metal components with high precision and accuracy.

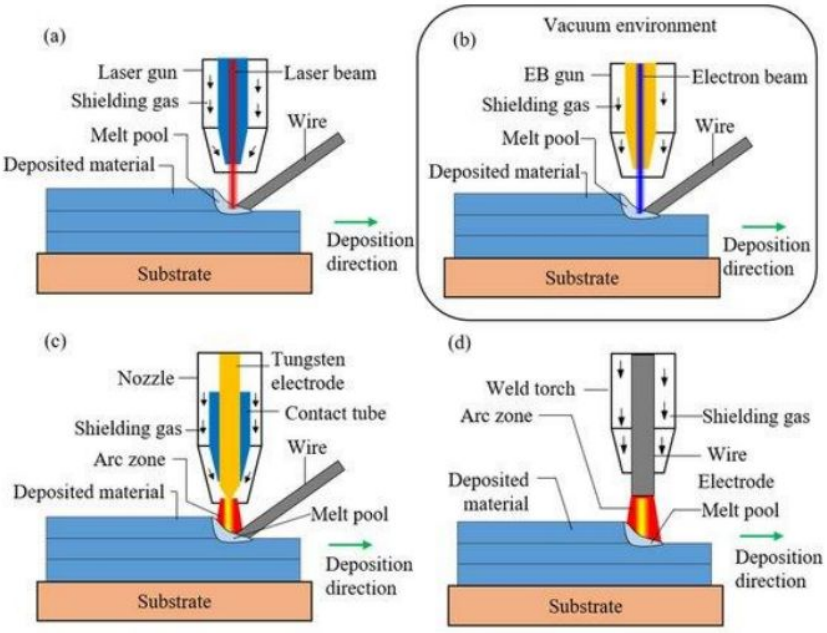

Fig. 1. 6 A schematic diagram of the wire-based technique: (a) WLAM; (b) EBF 3 ; (c) GTAW additive manufacturing; (d) GMAW additive manufacturing [12].

The innovative weld methods must be implemented to overcome the weldability problems and obtain defect free high strength multi material structures, e.g. adopting gradient transition of the two or more materials [13]. The different design modalities for FGMs developed in this work comprises of graded structures either throughout the entire material or only in some

localised regions. To test different FGM design strategies SS316L/IN625 can be a good choice as many researchers have attempted to fabricate FGMs and alloys using them. SS316L/IN625 alloys are majorly employed in high strain rate locations for reducing the plastic deformations, e.g., high-temperature resistant turbine blades, and missiles. FGM in gears incorporates wear-resistant materials at the surface and gradually transitions to a more ductile material towards the core, while also dissipating heat effectively to improve the gear's ability to withstand high thermal loads and extend its service life. Ship building and aerospace fields also have its usage due to the good joint strength and structural integrity.

Although additive manufacturing has numerous benefits, it is still difficult to produce components with the best desired physical and mechanical qualities [14]. It might be due to the layer-by-layer deposition of materials used in additive manufacturing, which can lead to differences in material characteristics across levels and even within the same layer. Researchers have used statistical optimisation methods to enhance the mechanical characteristics of materials produced by additive manufacturing to overcome this problem. Full factorial design [15], Taguchi design [16], Box- Benkhein design [17] and Central Composite Design (CCD) [18] are few methods that enable the assessment and optimisation of dependent variables with a minimal number of tests. Among them, Full factorial design and CCD have been effectively used to optimise process parameters and improve product quality in several disciplines, including materials science, chemistry, and engineering.

1.5. Research Gaps

1.5.1. Research gap for Module 1: FGMs of SS316L/IN625

To study the feasibility of functionally graded material for corrosion, high temperature and stress applications, the different strategies of composition can be introduced such as alternate material layers (sandwich type) and continuous material variation (gradient type). Limited literature was found on the development and characterisation of special multi-layered sandwich

FGMs. Further, WAAM based continuous gradient FGM and special multi layered sandwich gradient FGM was not found in the literature. Therefore, the presented experimental study aims to fabricate different types of SS316L/IN625 FGM using dual wire WAAM-TIG process. It includes designs such as varying the composition at certain weight percentage (CG-FGM) and change of material alternatively (SW-FGM) of desired thickness. Further, detailed investigation on microstructure evolution, elemental composition, distribution, hardness, and wear characteristics were performed in detail to assess the adopted design feasibility. The achieved controlled deposition and its transient properties shall find many applications.

1.5.2. Research gap for Module 2: Alloys of CCD-based SS316L/IN625

Despite the increased attention in twin wire arc additive manufacturing, there is a lack of research on how to use CCD to improve the mechanical characteristics of this hybrid material. To address this gap, this paper analysed the samples fabricated to interpret the behaviour of dependent variables such as hardness, bead width, bead height, COF, wear removal rate, scratch hardness and Fracture toughness. The findings of this research study may be implemented to optimise the mechanical properties of hybrid material (SS316L/IN625), resulting in the excellent material properties. Overall, this research paper provides valuable insights into the use of CCD for optimizing the mechanical properties of SS316L/IN625 hybrid material produced through twin wire arc additive manufacturing.

Chapter 2 Literature Review & Objectives

2.1. Literature Review

2.1.1. Overview

The fabrication of continuous gradient FGM by additive manufacturing (AM) technology has been examined previously in joining of Stainless steel/nickel-based super alloys, Ti/Ni alloys, Al/Al_2O_3 etc. CCD has shown a lot of potential in the field of additive manufacturing in improving the mechanical characteristics of materials. CCD may be utilised, especially to determine the ideal process variables that result in the desired mechanical qualities, limiting the number of trials necessary and reducing the total cost and duration of the optimisation process.

2.1.2 Literature Review for Module 1: FGMs of SS316L/IN625

Carroll et al., (2016) fabricated SS304L/IN625 FGMs by decreasing the volume of SS304L by 4% and increasing IN625 volume by the same amount in successive deposits for the transition zone using the directed energy laser deposition technique (LMD) process. They found that the microstructure changed progressively from austenite and ferrite phases to cellular dendrites and then to columnar dendrites as the content of SS304L decreasing at the same time IN625 increasing in the transition zone [19].

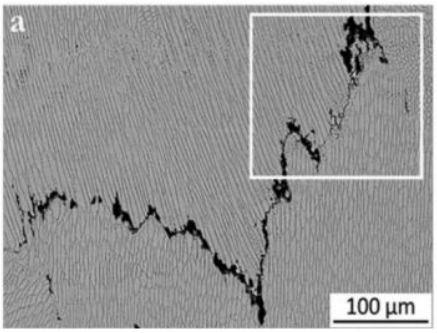

b	Design	Actual
Fe	54.6	56
Cr	19.8	20
Ni	21.1	18
Mo	1.8	2
Mn	1.1	1
Nb	0.7	1

Fig. 2. 1. crack observed having Nb and Mo content.

Meng et al., (2019) fabricated two FGMs of IN625/Ti6Al4V and SS316L/IN625 with 10% composition change using fibre laser metal

deposition (LMD) and conducted a study on microstructure and microhardness with/without preheating conditions. In IN625/Ti6Al4V, they found the cold cracks (smooth, straight, trans-granular propagation) at interface between the layers of 80% IN625/20% Ti6Al4V and 70% IN625/30% Ti6Al4V under no preheat condition due to presence of Mo and Cr rich hard and brittle phases. While in SS316L/IN625 sample, solidification cracks (crack distribution along the columnar crystal boundary) were generated. Based on EDS analysis, Mo and Nb elements found in inter-dendritic regions as $(Mo, Nb)_2C$ phase was the cause of crack formation [20].

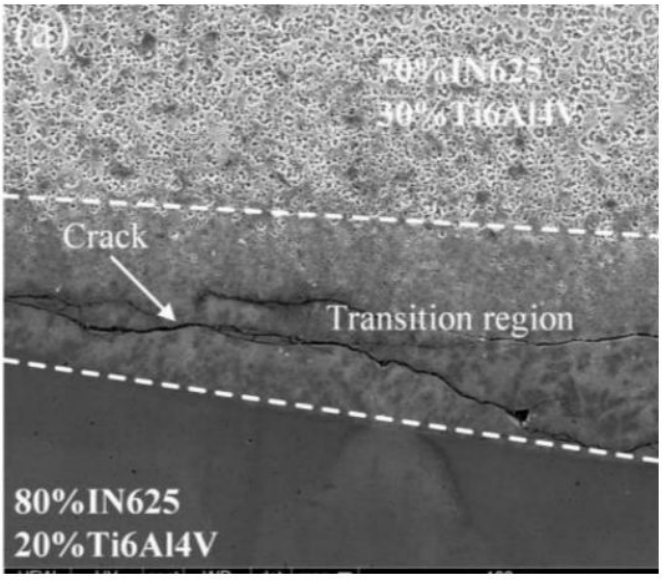

Fig. 2.2. cold and solidification cracks due to Mo and Cr rich hard and brittle phases

Rodrigues et al., (2022) fabricated Cu-Al alloy and HSLA steel-based transition step based FGM using TIG-based wire arc additive manufacturing technique. They found that there was a formation of large interface region leading to gradual change in mechanical and electrical properties [21].

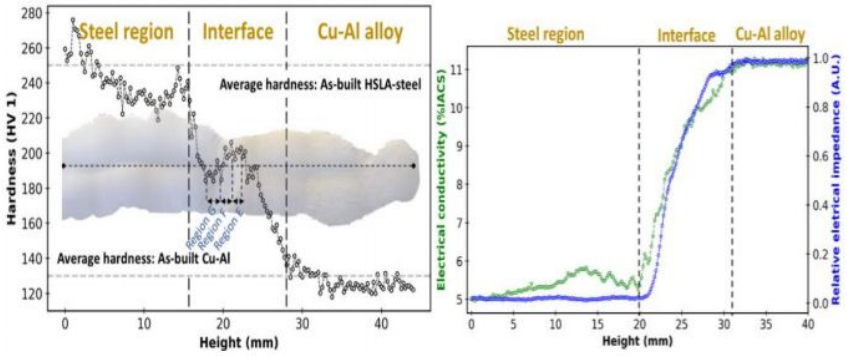

Fig. 2.3 Gradual variation of properties in graded region of Steel–copper FGM

Kumar et al., (2021) developed sandwich-type single-layered SS321/IN625 FGM using the WAAM-MIG. The variation in microstructure based on the build direction was observed as equiaxed and columnar dendrite structures in SS321, and fine columnar dendrites with secondary arms and precipitates in the IN625 region. They found the fractured locations have voids and few dimples [4].

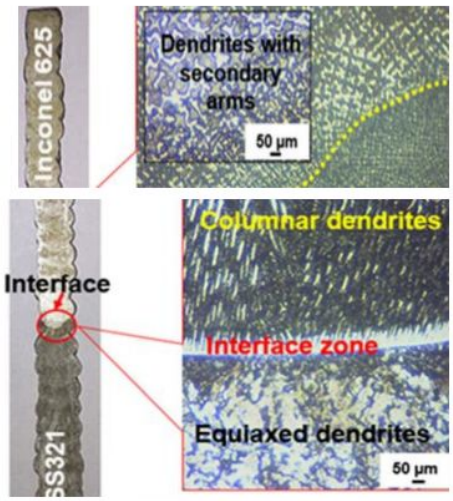

Fig. 2.4 Microstructure variation along graded region of FGM.

Bobbio.et.al., (2018) considered Wire Laser Additive Manufacturing (WLAM) for the fabrication of Vanadium/Invar 36 FGM. The sequence of fabrication is Pure V + V/Invar Continuous gradient FGM (3 % volume change/material) + Pure Invar. It was found that in V to Invar FGM, in range 18-52 vol% Invar cracks in graded zone were observed due to sigma-FeV brittle phases in 27-52% Invar results in hardness increase and cracking [23].

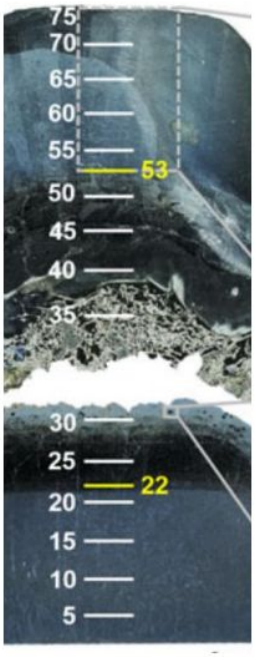

Fig. 2.5 Cracks observed in graded zone due to brittle phases.

Cunningham.et.al., (2018) reported the materials processing challenges WAAM by adopting various WAAM strategies to enhance the part quality. They found that the dominant mechanism of heat transfer for initial layers of deposition is reported as conduction whereas with increase in number of layers convection and radiation dominates. This variation in thermal profile occur when heat flux changes from steady state due to change in heat dissipation [24].

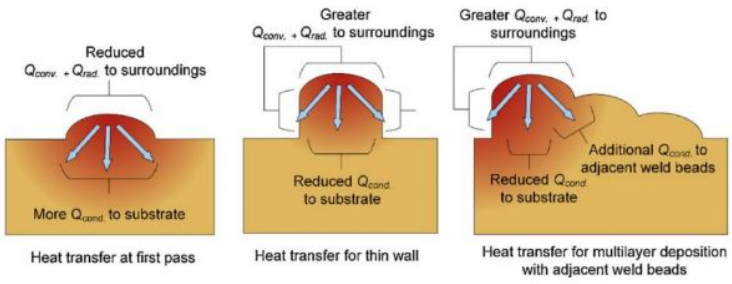

Fig. 2.6 Heat transfer behavior along the build direction of WAAM

The above literature suggests that attempts have been made by researchers in developing continuous graded, single-transition step, three-material transition and gradient metal matrix composite (MMC) using majorly LENS, LMD, and WAAM-MIG process. Considering the high energy efficiency

(~90%) in producing desired three dimensional parts comprising of different materials a WAAM-TIG [25] could also be a better choice [21]. WAAM-TIG enables thin-walled components fabrication with cost-effectiveness benefits. It allows consolidation of individual components into complex shapes. It can also improve geometric tolerance and fabricate functionally graded materials (FGM) with high strength-to-weight ratios.

It is crucial to understand the part deposition feasibility, precision, and dimensional accuracy to establish FGM standards in industries. Inconel 625 and SS316L have strain hardening tendencies, making it difficult to join using conventional processes.

2.1.3. Literature review for Module 2: Alloys of CCD-based SS316L/IN625

In the context of additive manufacturing, CCD has shown much potential in additive manufactu[r]ing in improving the mechanical characteristics of materials. CCD is ideal for modelling complex responses and capturing non-linear relationships. It enables exploring a wide parameter space while efficiently utilising experimental resources [26].

Khademzadeh et al., (2022) studied micro-laser powder bed fusion of Inconel 718 using a 30 μm laser spot, investigating mechanical behaviour and correlating it with microstructure. In the response surface method, CCD optimised process parameters to improve outcomes with maximum relative density and minimum surface roughness. The optimised parameters achieved 99.9% relative density, <10 μm surface roughness, and fine microstructure [27].

Imanian et al., (2022) investigated the effects of selective laser sintering (SLS-AM) variables on surface roughness and dimensional accuracy using CCD. They found that using CCD helped determine the appropriate input values to achieve the desired surface roughness and dimensional accuracy. The study also found that the surface roughness decreases with reduced layer

thickness, scan spacing, and laser speed but increases with reduced laser power [28].

Hosseinzadeh et al. (2023) developed a mathematical model using the response surface method (RSM) to control the amount of Polylactic acids (PLA) in the torsional and flexural deformation of 4D printing. According to their study, the CCD helped them in obtaining the optimum conditions for achieving maximum deformation and achieve the desired shape recovery in the bending and torsion modes [29].

Lu et al., (2022) used CCD to analyse the impact of SLM process parameters on the relative density and surface roughness of Inconel 718. CCD helped to achieve the prediction models and identifying optimal process parameters. Multi-objective optimisation balanced relative density and surface roughness. The relative density model showed the optimum values, i.e., mean absolute error (MAE) of 0.35, root mean square error (RMSE) of 0.43, and coefficient of determination (R^2) of 70.14%. Similarly, for the surface roughness model, the MAE is 1.07, RMSE is 1.37, and R^2 is 74.36% [30].

Zhang et al., (2023) studied the droplet transfer behaviour and stability of the swing arc additive manufacturing process of AZ91 magnesium alloy using cold metal transfer (CMT). CCD helped them in achieving a stable deposition process and improving the appearance of the defect-free deposited layer. The optimum combination of CMT characteristic parameters for the swing arc deposition process of Mg alloy was boost phase current of 312.5 A, boost phase duration of 2.5 ms, burn phase current of 10 A, and short-circuiting current of 75.5 A [31].

Raj et al., (2022) conducted an experimental investigation using the Central Composite Design (CCD) approach to analyse the flowability characteristics of a mixed powder of AlSi10Mg and NbC in a planetary ball mill. The adopted CCD helped them to determine the optimum combination of input parameters, such as mixing time, speed, and NbC composition, which resulted in improved flowability characteristics of the mixed powder. The overall result

showed the optimised combination of the mixed powder as AlSi10Mg + 8% weight of NbC [32].

Sayed et al., (2020) used a three-factor CCD design to examine the relation between the design parameters of additively manufactured lattice structures for biomedical implants and their compressive characteristics. CCD optimised lattice structure parameters for improved properties by balancing porosity, compressive strength, modulus, and ultimate strength. An optimised diamond lattice structure with specific compressive strength of 37.8 kN m/kg, elastic modulus of 1 GPa, ultimate compression strength of 49.5 MPa, and porosity of 85.7% was achieved [33].

Salih et al. (2023) attempted to enhance the mechanical qualities of a polymer resin used in stereolithography (SLA) 3D printers by including chopped carbon fibres. CCD-based design of experiments (DOE) revealed that using carbon fibre boosted ultimate strength to a peak that declined afterwards. Adding 0.25 wt% carbon fibre to a 30 µm printing layer increased tensile strength by 47.82%, but adding more carbon fibre decreased tensile strength [18].

Ghelich et al., (2019) optimised the electrospinning process to produce HfB_2 nanofibrous composites using a five-level five-factor CCD approach. CCD helped identify the most critical process variables, such as initial polyvinylpyrrolidone concentration and B/Hf molar ratio, for obtaining nanofibrous composites with a narrow size distribution. The study successfully synthesised HfB_2-based nanofibrous composites with excellent fibrillar morphology after heat treatment, as confirmed by XRD analysis [34].

2.2. Objectives

2.2.1. Objectives for Module 1: FGMs of SS316L/IN625

- To fabricate the different types of SS316L/IN625 Functionally graded materials using dual wire WAAM-TIG process.
- The presented study designs and analyse the various WAAM-TIG manufactured SS316L / IN625 FGMs by ensuring good material

adherence, high-quality performance towards mechanical and tribological properties.

- To validate the different adopted designs that includes the varying composition at certain weight percentage (CG-FGM) and change of material alternatively (SW-FGM) of desired thickness.
- Further, detailed investigation on microstructure evolution using optical microscopy and scanning electron microscopy.
- To validate the elemental composition, and their distribution along with dilution behaviour using EDS area scan and EDS mapping.
- To study the mechanical properties that analyses the hardness, and wear characteristics i.e., coefficient of friction (COF) and specific wear rate (mm^3 / length) to be performed in detail.
- To understand crystallographic planes, peaks, and peak heights at different regions of FGM consisting of various combinations of SS316L / IN625.
- Assess the adopted design's feasibility and their controlled deposition characteristics.

2.2.2. Objectives for Module 2: Alloys of CCD-based SS316L/IN625

- This research objective 2 investigates the use of central composite design (CCD) to enhance the mechanical characteristics of a hybrid SS316L/IN625 material manufactured using twin wire arc additive manufacturing.
- The different combinations of hybrid material designed need to be manufactured through layer-by-layer deposition of two wires of different materials i.e., SS316L and IN625.
- Central Composite Design (CCD) derived from design of experiments (DOE) was adopted and designed based on independent factors such as composition, current and travel speed.
- The response surface methodology models were analysed for various properties of the material to be developed.

- To optimize the dimensional accuracy of functionally graded material, the statistical models for bead width, bead height can be developed.
- Further to optimize mechanical and wear properties for application purpose, the hardness, coefficient of friction, specific wear rate, fracture toughness and scratch hardness models can be developed.
- To perform analysis of variance (ANOVA) on all response models and optimize it to accept or reject the null hypothesis based on p-statistic value of each factor.
- To optimize the R^2 value for each model among Linear, Linear + Squares, Linear + Interactions and Full quadratic types.
- To analyse the error distribution for each model with respect to runs or number of experiments.
- To perform the response optimization based on requirements i.e., minimise, maximise, and target the output parameter, and retrieve the corresponding input factors.

Chapter 3 Methodology and Experimental details

3.1. Methodology

Fig. 3.1 shows the pictorial view of the in-house developed WAAM-TIG experimental setup with tungsten inert gas (TIG) (Migatronics PI 350 AC/DC) machine as a heat source. Two individual cold wire feeders (Migatronics CWF multi) were used to feed the SS316L and Inconel 625 wires of 0.8 mm diameter into the stabilised TIG arc. The worktable was operated by a three-axis CNC manipulator [35]. A 5 mm thick mild steel (AISI1020) plate was used as substrate material. Argon gas was used at a constant flow rate of 10 L/min as inert gas. Tungsten electrode of diameter of 2.4 mm was placed at a constant stand-off distance (SOD) of 4 mm.

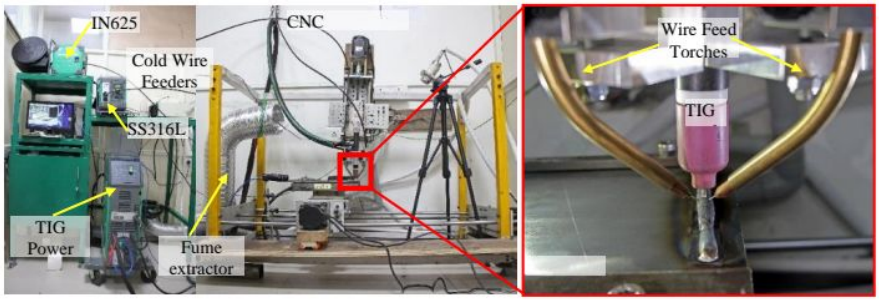

Fig. 3.1 Multi wire WAAM-TIG experimental setup utilised for fabricating FGM showing various components, along with the two wire feed torches setup showed in inset.

Fig. 3.1b shows the enlarged view of the typical experimental arrangement for dual wire feed system. The dedicated fixtures were used for positioning and directing the wires through two wire-feed torches. In general, the front feeding is preferred due to better dimensional accuracy [36], however, accommodation of the two wire feed torches in the front would be difficult. Therefore, the wire feed torches were fixed at an angle of 35° each from the front with respect to the axis of deposition. This helped in ensuring the feed direction closer to the standard front-feeding while accommodating the wire feed torches. This arrangement led to continuous and uniform bead deposition (Fig. 3.1b).

3.2 Experimental details (Module 1)

3.2.1. Overview

The two wires were fed simultaneously at different speeds to achieve the desired composition for each layer. Table 2 represents the different elemental composition associated with the chosen SS316L and IN625 materials. Two different characteristics of FGM has been employed to deposit multilayer straight walls.

3.2.2. Continuous gradient FGM (CG-FGM)

In CG-FGM cumulative wire feed speed (wfs) of 4 m/min was maintained constant while feeding individual wires. A total of 22 layers has been deposited with an increment/decrement of 10% in composition after every two layers for IN625 and SS316L, respectively. So, the composition of SS316L will be 100% at the bottom and 0% at the top and vice-versa for IN625. Table 1 incorporates the required wfs associated with both the materials for individual layers. It also incorporates the obtained average layer thickness and cumulative height achieved.

Table 1 CG-FGM composition for each layer.

No of layers	wfs-SS316L (m/min)	wfs-In625 (m/min)	Average layer thickness (mm)	Cumulative height (mm)
1-2	4.0	0	2.0	4
3-4	3.6	0.4	1.6	7.2
5-6	3.2	0.8	1.7	10.6
7-8	2.8	1.2	1.3	13.2
9-10	2.4	1.6	1.0	15.2
11-12	2.0	2.0	1.4	18
13-14	1.6	2.4	1.5	21
15-16	1.2	2.8	1.4	23.8
17-18	0.8	3.2	1.4	26.6
19-20	0.4	3.6	1.3	29.2
21-22	0.0	4.0	1.5	32.2

3.2.3. Sandwich Type FGM (SW-FGM)

In the case of SW-FGM, the individual layers of SS316L and IN625 were deposited alternatively. The bottom layer consisted of 100% SS316L and 0% IN625, which varied alternatively to 0% SS316L and 100% IN625 for the desired number of layers ensuring 100% IN625 at the top layer. So, for every layer the material changes with a small fusion zone. The deposited samples are represented as ABAB for single-layer, AABB for double-layer, and AAABBB for triple-layer SW-FGMs, where A represents SS316L, and B represents IN625. The input parameters details for these structures are presented in Table 3. The alloying effect in SW-FGM with different design modalities and its comparison with '50% A and 50% B' weight percentage deposition was also studied, and the deposition parameters is included in Table 1.

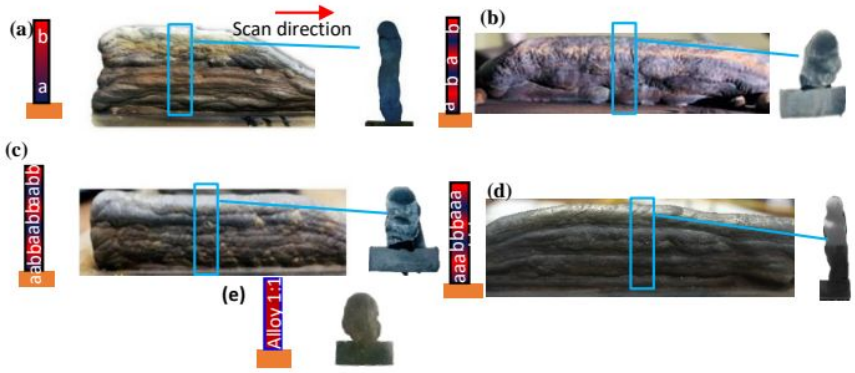

Fig. 3.2 (a) CG-FGM sample (10% increment/decrement of SS316L/IN625), (b), (c), (d) SW-FGM samples with different set of layers i.e., 1,2, and 3 layers of each material (SS316L/IN625) along the build direction respectively and (e) Alloy of SS316L/IN625 with 50 % composition of each material.

Table 2. Composition of two materials opted for FGM fabrication

	Fe	Ni	Cr	Mo	Mn	Si	C	P	S	Al	Ti	Co	Nb
SS316L	65.64	12	17	2.5	2	0.75	0.03	0.045	0.03	-	-	-	-
IN625	5.0	58.47	21	9	0.5	0.5	0.1	0.015	0.015	0.4	0.4	1	3.6

After the deposition, the walls were cut across the cross-section using wire EDM and standard mounting and polishing procedures were followed for microstructural, mechanical and tribological study. To exhibit the microstructure, electrolytic etching was performed in 10% oxalic acid at 6 V for a duration of 5 sec. Additional etching of ~45 sec was observed to be required for prominent revealing of microstructures containing the SS316L weight percentage near 100%. After the sample preparation, microstructure of the cross-section was observed in optical microscope (Leica DFC295) and Scanning Electron Microscope, SEM (JEOL 7610F plus) equipped with Oxford energy dispersive spectroscopy (EDS). Elemental analysis was performed to find the variation in composition. Micro-indentation hardness was measured at different locations along the deposition height using Vickers hardness tester (Mitutoyo HM-210 Type A). Linear reciprocating wear test was performed using with 0.6 mm tungsten carbide (WC) ball diameter, 20 Hz frequency, 3-6 mm stroke length and 10 min of time duration.

Table 3 Optimised Parameters of deposited walls of CG, SW-FGM and Alloy

	CG-FGM		SW-FGMs		Alloy
	Sample 1 (10 % increment)	**Sample 2 (ABAB..)**	**Sample 3 (AABB….)**	**Sample 4 (AAABBB…)**	**Sample 5 (50:50)**
Total WFS (m/min)	4.0	3.0	3.0	3.0	4.0 (2:2)
Current (A)	170	120	120	120	212
Travel Speed (m/min)	0.2	0.2	0.2	0.2	0.2
No of layers deposited	22	10	12	18	8

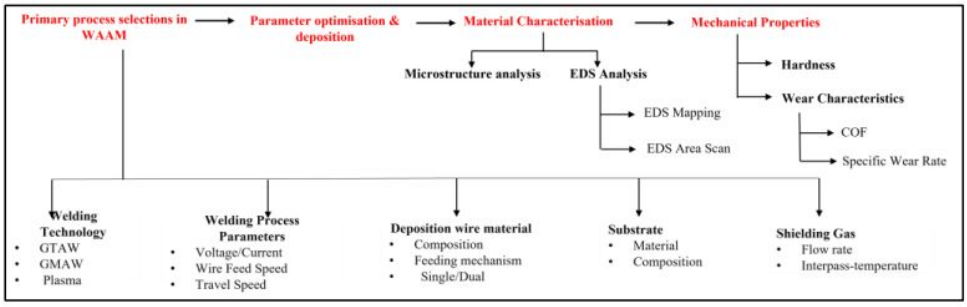

Fig. 3. 3 Methodology for fabrication and analysis of FGM

3.3. Experimental details (Module 2)

3.3.1. Overview

The research study was conducted using an in-house built TIG based twin-wire WAAM-TIG setup to perform the experiments. The setup consisted of a tungsten inert gas (TIG) power source, two separate cold wire feeders, and a 3-axis CNC manipulator. The base substrate material used was AISI-1020, which underwent polishing and cleaning with acetone to ensure a clean, flat, and particle-free surface. The SS316L and IN625 wires had a diameter size of 0.6 mm each. Front feed was employed for both the materials with a small offset of 35°. The wire fees speed (wfs) of 4 m/min was constant throughout the experiments. Further a statistical study was conducted on the data collected through various tests.

3.3.2. Design of experiments

A central composite design response surface method was used to design the experiments (DOE). The chosen input factors were alloy composition (SS316L:IN625), arc current (A), and travel speed (mm/min), while the responses were hardness, bead width, bead height, coefficient of friction (COF), wear removal rate, scratch hardness and fracture toughness. A total of 5 layers were deposited for each combination of input variables corresponding to 20 SS316L/IN625 samples. After the experimental implementation and the characterisation, the responses obtained were used to analyse the response surface design. The regression models for every response were fitted to the experimental data to estimate the main effects, interactions, and quadratic effects of the input factors. The regression equation takes the form:

$$Y = \beta_0 + \beta_1 C + \beta_2 I + \beta_3 S + \beta_{12} CI + \beta_{13} CS + \beta_{23} IS + \beta_{11} C^2 + \beta_{22} I^2 + \beta_{33} S^2 + \varepsilon$$

Here, Y represents the response variable, C, I, and S denote the symbols for the factors, β_0 is the intercept, β_1, β_2, β_3 are the linear coefficients, β_{12}, β_{13}, β_{23} represent the interaction coefficients, β_{11}, β_{22}, β_{33} signify the quadratic coefficients, and ε denotes the residual error term.

3.3.3. Statistical Model Terminology

To assess the quality of the regression models, various statistical indicators were examined. The coefficient of determination (R^2) measured the proportion of the total variance in the response variable accounted for by the regression model. A higher R^2 value indicates a better fit. Furthermore, a normal probability plot was employed to verify the assumption of normality for the residuals. Offset from the straight line on the plot may indicate deviations from normality. In addition, analysis of variance (ANOVA) was conducted to evaluate the significance of the regression model and assess the adequacy of the model in explaining the observed variation in the response variable. ANOVA comprises the model sum of squares (SS-model), which demonstrates the effectiveness of a model in representing its data, and a non-

significant lack of fit indicates that the model describes a good relationship between factors and response variables. The degrees of freedom (df) were also calculated, which is the total number of observations minus the number of predictors (responses). The F-statistic is calculated as the ratio of the mean square of the regression (MSR) to the mean square of the residuals (MSE). The F-statistic follows an F-distribution, which is a probability distribution used for hypothesis testing and analysis of variance, with specific degrees of freedom providing information about variability within and between groups. The P-value associated with the F-statistic is used to determine the statistical significance of the regression model. If the P-value is below the significance level (<0.05), it indicates that at least one factor in the model significantly impacts the response variable, leading to the rejection of the null hypothesis and supporting the statistical significance of the regression model and its relationships with the factors and the response variable. By performing hypothesis testing, ANOVA provides a robust statistical framework for evaluating the significance of the regression model in Central Composite Design (CCD) analysis.

Afterwards, a comprehensive analysis of the effects of input factors on the response variables was performed. This analysis used factorial and surface plots to better understand the relationships between the input factors and the responses. Factorial plots provide graphical representations of the main effects and interactions. Each input factor is plotted on the x-axis, while the response variable is displayed on the y-axis. The magnitude and direction of the main effects can be discerned by observing the slopes of the lines connecting the levels of each factor. On the other hand, the surface plots enable the visualisation of the response variable as a function of two factors, with the remaining factors held constant. Shape of the surface helped in determining the nature of the relationship between the input factors and the response variable. Peaks or valleys on the surface plot highlight optimal or suboptimal factor combinations. This optimisation process can be achieved by setting a specific target for the response variable or aiming to maximise or minimise it. Various techniques, such as the desirability function or

numerical search algorithms, such as gradient search, are employed for this purpose. The desirability function assigns desirability values ranging from 0 to 1 to different regions of the response surface. Higher desirability values indicate more desirable and accurate factor combination values. Table 5. Shows the measured responses for CCD designed specimens.

$$No\ of\ experiments\ (E) = 2N + 2N + R = 23 + 2 * 3 + 6 = 20 \quad (1)$$

$$Y = \alpha 0 + \sum \alpha ixi + \sum \alpha iixi2 + \sum \alpha ijxixj + \varepsilon \quad (2)$$

$$MS = \frac{\text{Sum of Squares (SS)}}{\text{Degrees of freedom (DOF)}} \quad (3)$$

$$\text{F ratio} = \frac{\text{Mean of Squares between (MSv)}}{\text{(Mean of squares within (MSe))}} \quad (4)$$

$$DOF = \text{No of variable groups} - 1 \quad (5)$$

$$\text{Sum of Squares within, SSW} = \sum(Yij - Yi.avg)2 \quad (6)$$

$$\text{Sum Of Squares} = \sum(Yi.avg - Ytot.avg)2 \quad (7)$$

Where N represents no of independent factors, R denotes no of repetitions, and Y_{ij} denotes the ith observation of the ith group.

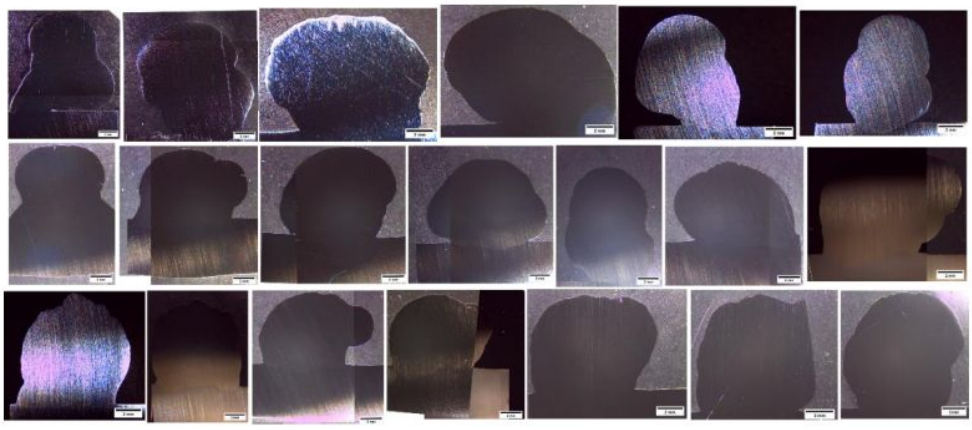

Fig. 3.4 Stereo micrographic cross-sectional images of 20 samples designed with CCD design of experiments.

Table 4 Design matrix with factors and coded levels used in central composite design (CCD)

Variable	Symbol	Unit	Coded variable levels		
			-1	0	1
Composition	C	No unit	1:3	2:2	3:1
Current	I	Amp	170	212	254
Speed	V	mm/min	100	150	200

Table 5 CCD designed experimental runs showing experimentally measured response value.

Run	Composition (SS316L: IN625) %	Current (A)	Speed (m/min)	Max. bead width (mm)	Effective bead width(mm)	Bead height (mm)	Hardness (HV)	Fe	Ni	Sp. Wear Rate (mm^3/length)	COF	Fracture Toughness	Scratch hardness
1	75:25	170	100	11.56	7.02	11.5	160.54	49.72	22.46	0.053800	0.3622	4.00492	2.62275
2	25:75	170	100	11.75	6.22	11.5	200.29	18.33	48.78	0.024713	0.6531	4.60731	3.04583
3	75 : 25	254	100	12.55	9.09	8.90	162.95	55.72	19.39	0.086600	0.4167	3.73003	2.45099
4	25 : 75	254	100	13.23	8.42	9.00	192.07	25.58	43.29	0.134540	0.5758	5.63930	3.34728
5	75: 25	170	200	7.94	4.14	8.50	168.69	56.20	21.67	0.069667	0.3521	4.40217	2.96503
6	25 : 75	170	200	7.12	4.57	8.81	207.76	21.82	44.55	0.107267	0.4499	3.94065	2.45644
7	75 : 25	254	200	9.77	7.73	7.00	162.17	57.27	18.54	0.091267	0.6234	4.50396	2.53218
8	25 : 75	254	200	10.37	8.68	6.68	200.3	26.60	50.03	0.146800	0.4440	4.09450	2.70126
9	75 : 25	212	150	10.78	8.28	8.5	160.45	52.50	21.43	0.097267	0.7098	5.46543	3.30694
10	25 : 75	212	150	11.86	7.82	8.3	199.87	39.60	37.85	0.104600	0.5004	4.27108	2.99054
11	50 : 50	170	150	8.70	7.15	11	186.073	33.27	32.93	0.127800	0.6520	4.67145	2.90664
12	50 : 50	254	150	11.03	9.17	7.18	183.76	39.34	30.4	0.132333	0.4089	4.83049	2.94523
13	50 : 50	212	100	11.41	7.75	8.90	185.12	35.25	35.9	0.139800	0.8786	3.37683	2.37883
14	50 : 50	212	200	8.67	7.28	8.55	186.17	34.7	32.25	0.097933	0.7160	5.00332	3.35489
15	50 : 50	212	150	8.99	8.32	9.38	194.65	37.15	39.63	0.130933	0.7213	3.52626	2.99834
16	50 : 50	212	150	10.79	7.74	7.36	214.01	37.5	35	0.071800	0.8080	4.06843	2.58035
17	50 : 50	212	150	10.10	8.06	7.59	186.4	37.7	33.9	0.122400	0.9263	4.13828	2.48084
18	50 : 50	212	150	10.02	7.86	7.69	187.69	35.75	32.35	0.053800	0.6580	4.00492	2.62275
19	50 : 50	212	150	8.83	7.31	8.77	180.86	35.3	33.53	0.024713	0.5670	4.60731	3.04583
20	50 : 50	212	150	10.73	8.41	9.42	184.91	36.57	32.73	0.086600	0.7150	3.73003	2.45099

Chapter 4 RESULT AND DISCUSSION (Module 1)

Different design strategies of FGM

4.1. Optimisation of deposition parameters

Optimisation of deposition parameters were performed to obtain uniform and smooth deposition of the weld bead. Parameters such as wfs, arc current, deposition speed and wire alignment were optimised. The wires were adjusted so that they will meet at a point on the axis just below the tip of the tungsten electrode to get smooth bridge transfer of the material. The deposition speed was kept constant at 0.2 m/min. The minimum possible wfs required for the continuous uniform deposition was found to be 0.3 m/min, below which the material transfer could not take place. It could be because of the high surface tension of the molten metal at the tip of the wire restricting the detachment. Therefore, the minimum wfs of 0.4 m/min has been considered in this study as illustrated in Table 1. The maximum wfs selected was 4 m/min. To keep the current constant throughout the experiments for the selected rage of other parameters the experimentally found current was 170A. Inter-layer temperature below 100°C was maintained as confirmed by measuring the cooling cycle using non-contact temperature sensor (pyrometer, IGAR6 advanced).

4.2 EDS analysis

The fabricated FGM showed good fusion for SS316L and IN625 deposited wall. Macrostructural images of continuous and sandwich structured FGMs is presented in Fig 3.2. EDS area scan was performed along the build direction to analyse the variation in composition of major governing elements i.e., Fe, Ni, and Cr. An area of 0.5x0.5 mm2 at a regular interval of 0.5 mm was scanned in a straight line lying at the centre of the deposited bead as shown in the schematic of Fig. 4.1a. Fig. 4.1b-e also shows the found weight percentage of Fe and Ni for the deposited CG-FGM and SW-FGM walls.

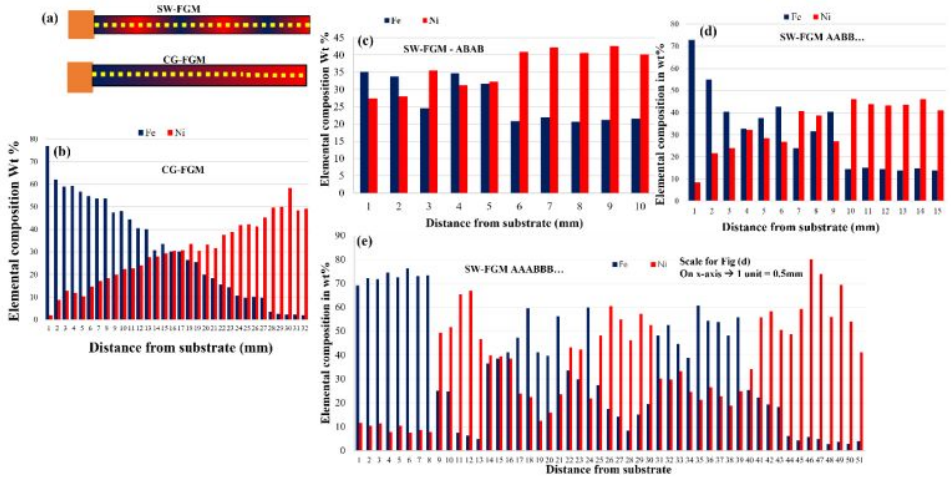

Fig. 4.1 Elemental composition of the FGMs along the wall height (a) schematic showing area scan strategy, (b) CG-FGM, (c-e) SW-FGM.

In the case of CG-FGM, a gradual decreasing and increasing trend was found for Fe and Ni, respectively (Fig. 4.1b). The first layer is supposed to be composed of 100% SS316L which have an Fe content of ~66%, however, it was found to be 77%. Fusion of first layer with Fe dominant substrate might be the possible reason for this behaviour. It also affected the Ni content in the first layer, which was found to be ~1.8%. As the weight percentage for IN625 was increased from the third layer onwards, the Ni content was observed to be increasing. In the middle region when the weight percentage for both the materials were same, the Fe and Ni content were found to be similar at ~30%. In the top region, the Ni content was found to be more as expected, as the weight percentage of IN625 has increased. The Cr content was found to be constant at ~17% over the entire regions of sample produced.

SW-FGM with a single layer alternate material showed no substantial change in composition along the building direction. For the initial layers, the EDS area scan analysis showed the complete alloying trend (Fig. 4.1c). Further, the double-layered SW-FGM exhibited varying Fe and Ni content, with three peaks recorded for each (Fe: 1-2, 6, 9; Ni: 4, 7, 10-15). This falls in-line with the desired composition, i.e., two layers of each material deposited alternatively (AABB…, Fig. 4.1d). Owing to alloying behaviour in the last few layers of the deposition for the double layered SW-FGM, the triple

layered SW-FGM was chosen as the next sample for the examination. The triple-layered SW-FGM displayed distinct sharp peaks and valleys of Fe and Ni along the build direction, showing a high degree of correlation of sample with the desired design (Fig. 4.1e).

The dominant mechanism of heat transfer for initial layer of deposition is reported to be conduction whereas with increase in number of layers convection and radiation dominates [24]. Further the arc pressure and acting gravity are also the matter of concern in order to understand the behaviour of peak shifting towards downward found in the EDS graph [35]. Since the initial layers of SS316L were deposited on a mild steel substrate the high peaks of the Fe is as expected. With the further layers of IN625 deposition on already deposited SS316L wall, the dilution is expected to be relatively high. In the case of TIG arc based WAAM, the arc intensity melts the previously deposited layer at the same time the arc pressure and gravity acts in a downward direction forcing the Ni elements to penetrate deeper in a bath of melt pool. However, with the deposition of second layer of the same material the Ni content is expected to be high. The increasing trend of Ni content in initial layers evident the same. The increasing trend of Fe and Ni deposited in alternate sets in further layers also followed the similar trend as found in the EDS graph. For the last two sets of ABAB… and AABB… deposition, Ni was found dominating over Fe by a large margin. Again, the low cooling rate due to high heat accumulation caused bigger melt pool, however the Fe from previous layers could not move upwards against gravity. Here, the trend was found to be constant for Fe and Ni. Therefore, in the top region, partial alloying of both the materials were observed despite the deposition of pure material in successive layers. This could be further understood by three layer alternate material deposition (AAABBB…) performed for three sets yielding to 18 layers of the deposition (Table 3). Here, the transition zone and alloying effect could be prominently observed when materials changing alternatively. This transition zone was initially confined to limited region which tends to be increased for the next two sets of the deposition. The above results showed that to achieve the sandwich type of composition, the AAABBB strategy for

the deposition could be employed. The conducted experiments revealed that the single and double layer alternative material deposition, strategy led to complete and partial alloying of the materials respectively in all the regions. With three or more number of successive layer deposition, the distinction of the peaks could be more prominent and might extend to the top region. It could be because of, in the case of WAAM-TIG the dilution length or the interface is relatively larger (Rodrigues et al., 2022). However, employing other methods of additive manufacturing such as WAAM-MIG [5,22] and laser engineered net shaping (LENS) processes, where the free flight transfer of molten material is the dominant mechanism of material deposition the dilution length is reported relatively lesser [6].

Additionally, analysing the elemental mapping of interface helped in understanding the dilution behaviour of materials at the interface. Fig. 4.2a shows the substrate interface for SW-FGM.

The substrate regions majorly comprised of Fe with a very low composition of Ni and Cr (Khan and Madhukar, 2022). An interface zone of ~1 mm thickness was formed on the substrate, where the Fe remains dominating. After the interface i.e., in the first layer, all three major elements are equally present for a very narrow zone.

Further the Fe starts to dominate again as the first layer is formed by SS316L (as shown in Fig. 4.1b). Fig. 4.2b shows the layer interface of SS316L and IN625 in the middle region of SW-FGM. The transformation between the Fe and Ni at the interface was found to be gradual. It indicates the uniform fusion of IN625 and SS316L.

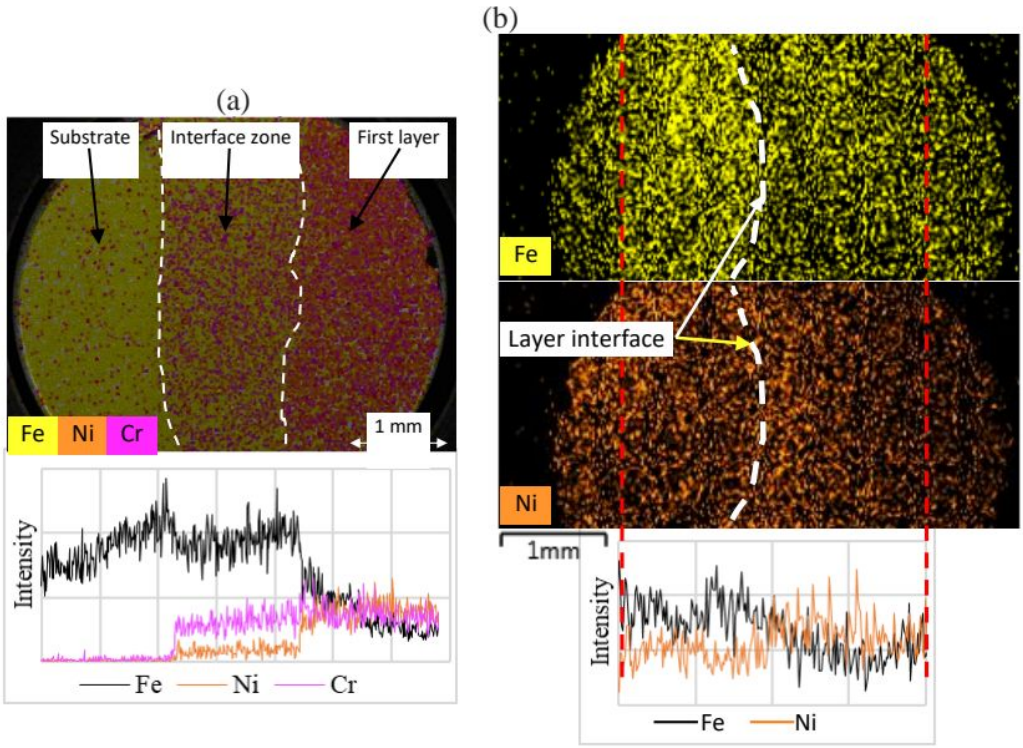

Fig. 4.2 EDS elemental mapping of (a) substrate-SS316L interface, (b) IN625-SS316L interface

4.3 Microstructure study

The microstructures of WAAM deposited SS316L and IN625 were predominantly cellular and columnar with cellular dendritic structures, respectively. Optical micrographs of CG-FGM illustrates the existence of layer-interfaces (Fig. 4.3a-f). Dendritic grain growth was found to be inclined to the vertical (along the solidification direction) in most regions following the largest temperature gradient resulting from heat dissipation through wall surface. Due to the convective heat transfer from the side and top surfaces, the grain growth direction was directed outwards to maintain high temperature gradient near the boundary regions. This behaviour was confirmed from SEM images (Fig. 4.3g-k). Similar trend was observed near the substrate as the conduction heat dissipation takes place through the substrate (Fig 4.3). The microstructure of IN625 varies based on the solidification rate and heat transfer during the deposition. Columnar dendritic structure occurred in the major region except in some of the bottom layers and near the boundaries due to rapid solidification. The low solidification rate

of the remaining layers due to continuous heating resulted in the nucleation and growth of columnar dendrites by remelting the equiaxed cellular grain [37], frequently observed in WAAM [38]. The variation in density of columnar grains (inter columnar spacing) was observed, as IN625 compound varies in the chemical composition. The grain density increases with increase in Inconel content and dendrites start extending along the build direction. In few regions, the interface between the two layers was evident with the sudden change in grain density (Fig. 4.3b).

CG-FGM: Epitaxial grain growth was observed as crystal growth direction of the microstructure between two consecutive layers was found to be similar. Long coarse columnar grains were present in the top layer which would act as the nucleation site for further layers. It could be formed due to high heat accumulation. In the central region, combination of fine columnar and cellular grains due to equal composition of both the materials was observed. Bottom layer just above the substrate showed cellular grains due to presence of 100% SS316L and high cooling rate.

The coarse columnar dendrites in the top region were found to be ~10 µm in width and 65 µm in length when measured using image-based processing software. The in graded zone the formed fine columnar dendrites were observed to be ~4 µm in width. In the bottom region, cellular grains were ~10 µm in diameter and ~12 µm inter-dendritic spacing. Here, short dendrites were also found in few regions which have 4-5 µm width and ~35 µm length. To summarise, the transition of grain structure from (cellular grains + short dendrites) to (fine + equiaxed) and then to (coarse + secondary arm) columnar dendrites was observed along the build direction. As a result, multiple microstructures are formed at different regions exhibiting in variation in mechanical properties along the build direction.

SW-FGM: Optical micrographs of SW-FGM illustrates the existence of layer-interfaces (Fig. 4.4). For bottom and middle regions, the distinct regions were observed for SS316L, IN625 and their transition. The layer interface extended over a large area with 60-70% overlap of the two materials deposited

consecutively. It showed good metallurgical bonding at the layer interface with little defects/cracks. The continuous heating of the layers by excess arc energy would remelt the pre-deposited material allowing the elements present in IN625 to penetrate the SS316L from top to the bottom layers. It formed an alloy in about one-third portion of a single deposited SW-FGM. The blending of SS316L and IN625 contributed to both equiaxed and columnar dendritic structures in intermediate regions of width ~300 µm. These microstructures have been reported pursuing higher strength compared to casted products [39]. For SS316L-IN625 interface, the middle regions had combined equiaxed and columnar structures while the top region was dominated by columnar structure.

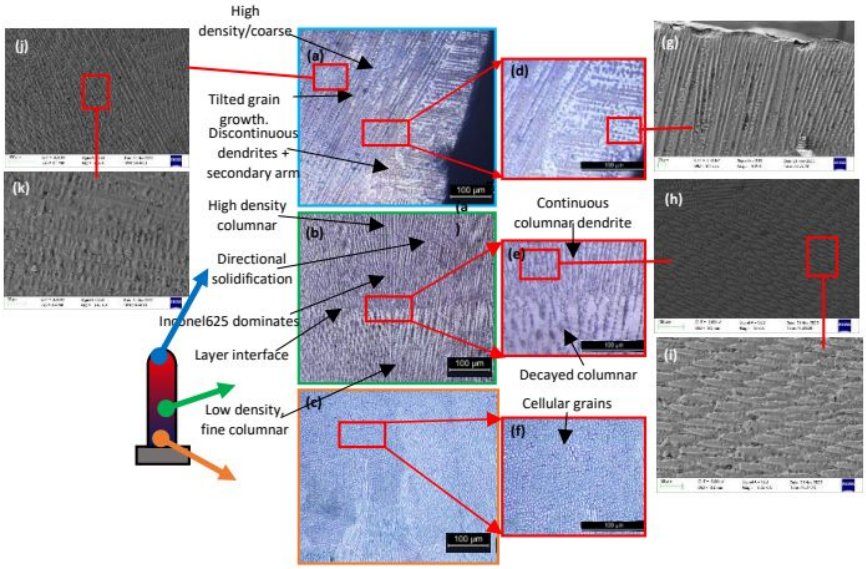

Fig. 4.3 (a-f) Optical and (g-k) SEM micrographs of CG-FGM for top middle and top regions.

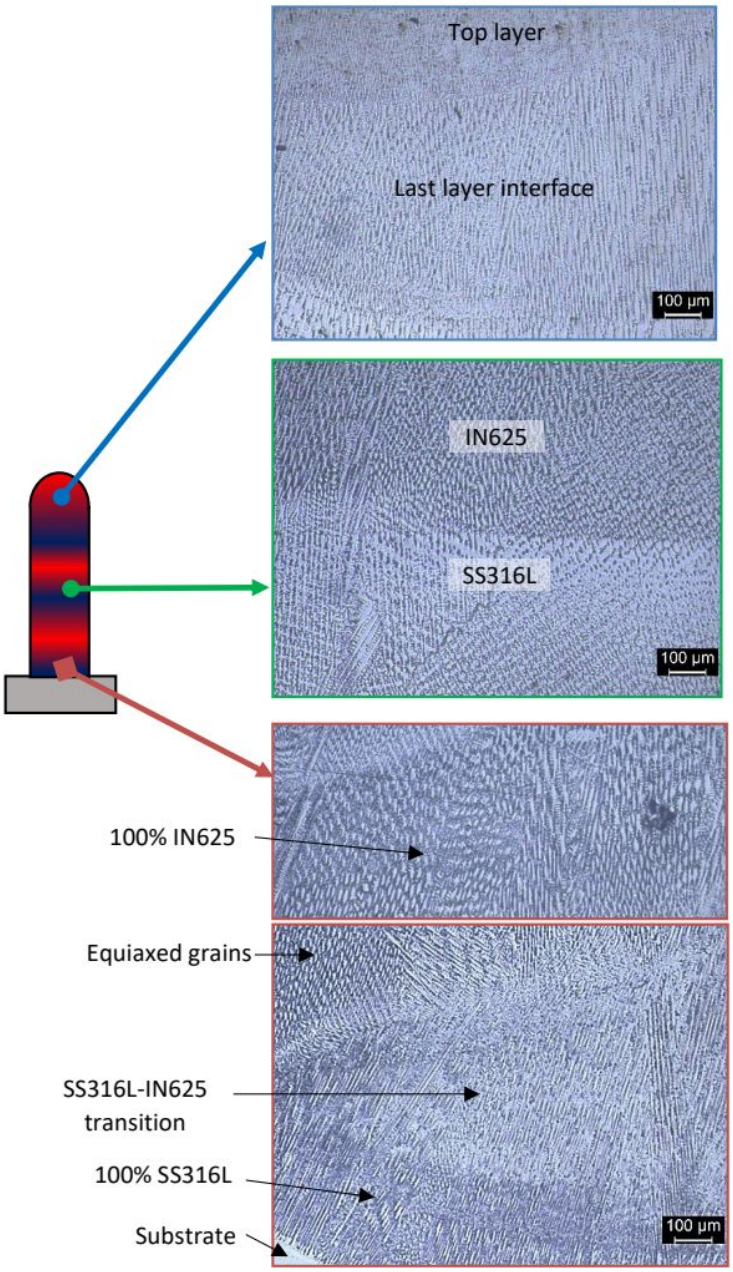

Fig. 4.4 Optical micrographs of SW-FGM (ABAB..) for top, middle, and bottom regions.

4.4. XRD analysis

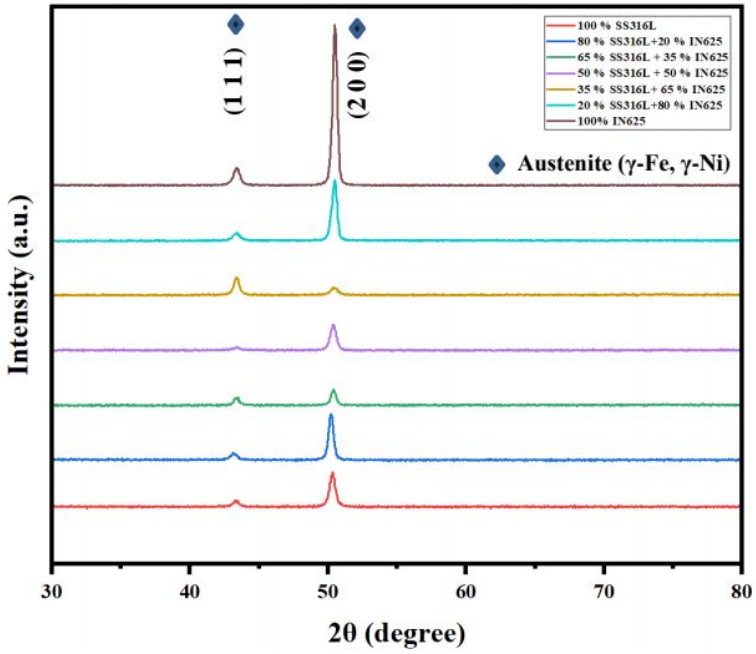

Fig. 4.5 XRD patterns in graded layers of SS316L/IN625 CG-FGM

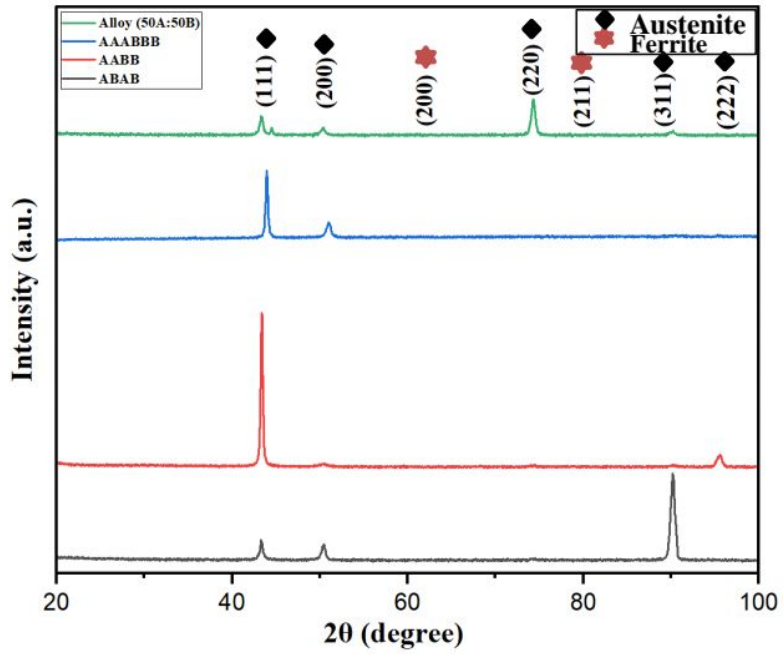

Fig. 4.6 XRD patterns in SS316L/IN625 Sandwich-FGM (AABB…) showing SS316L (bottom region) and IN625 (top region) dominated regions.

The X-ray diffraction (XRD) patterns were examined for various locations of the SS316L/IN625 FGMs along the build-direction fabricated using dual wire WAAM-TIG process. The objective was to analyse and compare the crystalline structure of the graded regions with the constituent metals. The two extreme ends, i.e., the bottom and top layer of the FGM, contained 100% SS316L and IN625, respectively.

The found XRD patterns for CG-FGM is presented in Fig. 4.5 and was in accordance with the additively manufactured pure SS316L and IN625 as reported by [40], [41]. It could be noticed that XRD possess broad focus (~3 mm diameter), therefore, every measurement could be considered scanning three to four layer of the deposition. Here, the deposited SS316L revealed negligible ferrite content, and the deposited IN625 exhibited an austenitic structure. The findings of this study were consistent with previous research revealing that both pure SS316L and IN625 contained the face-centred cubic (FCC) structure of the austenitic phase [42], with a small fraction of body-centred cubic (BCC) structure of ferrite [43]. Yen et al., 2008 have concurred with this assertion and have further identified the matrix as a γ phase, characterised by its high solubility of Fe.

The gradient zone displayed a uniform crystalline structure, as evidenced by the absence of changes in peak position despite an increase in IN625 content. Due to the low content of secondary phases or intermetallic compounds, these phases were not detected [44–46]. The gradual increase in the peak height could be correlated with the microstructural evolution from equiaxed and cellular SS316L grains to long fine columnar dendrites of IN625 [47,48]. The differences in peak heights can also be correlated with the hardness variation in the transition range of CG-FGM. The IN625 region of CG-FGM with high textured columnar dendrites resulted in a relatively high peak height at the (2 0 0) plane, resulting in higher hardness [49]. On the contrary, for SS316L, the peak heights of the (1 1 1) and (2 0 0) planes were lower and higher, respectively [50]. This resulted in a greater possibility of residual stress formation at the transition zone between the equiaxed grains and columnar

dendrites. The weight fraction of IN625 in SS316L caused a linear variation in hardness as the concentration of IN625 in SS316L increased can be observed in Fig. 16a. The EDS analysis exhibited an increase in the combined Neobium (Nb) and Molybdenum (Mo) content measured from SS316L (bottom region) to IN625 (top region) as represented in Fig 4.7. This corresponds to the gradual increasing trend of micro hardness from SS316L to IN625 region [51].

The found XRD patterns for the SW-FGM samples with the ABAB... and AABB... designs exhibited no significant variation in peak locations, indicating a crystalline structure of homogeneous type, dominated by austenite phases as presented in Fig 4.6.

In AABB... and AAABBB… designs the found peaks were identical to the CG-FGM design, whereas in ABAB... design few more peaks were observed. The XRD patterns revealed characteristic peaks of the austenite phase, including (111), (200), (220), (311), and (222), and additional minor peaks that corresponded to the ferrite phase, including (200) and (211). Typically, pure SS316L and IN625 materials reveals γ-Fe-Austenite (FCC), and γ-Ni (FCC) respectively. However, XRD patterns of alloy showed two peaks corresponding to (111) plane possibly due to the substrate involvement. The (111) peak also indicates the presence of a texture in the microstructure of SW-FGMs, revealing that most of the crystals have the same orientation and eventually form a specific mixed crystal structure. The (311) peak in SS316L/IN625 corresponds to the (311) plane in the austenite phase, which is associated with the interplanar spacing of the atomic planes in the FCC crystal structure. The (200) and (220) peaks in the austenite phase and the (200) and (211) peaks in the ferrite phase are related to the spacing of atomic planes in FCC and BCC crystal structures, respectively. The minor peaks observed suggest the presence of a little ferrite phase in the SW-FGMs.

Fig. 4.8 showed the average grain size of CG-FGM from pure SS316L region to pure IN625 region. The average grain size was calculated by using Debye–Scherrer equation in XRD analysis [52]. Average grain size was found to be

in the range of 15 and 20 nm for the CG-FGM. According to the data, the grain size of the material tends to increase from the bottom layer to the top layer, with minor fluctuations in between. These findings imply that the material's composition shift may be contributing to the steady rise in grain size. The presence of IN625 and its columnar dendritic structure may be responsible for the variation in average grain size. Overall, the numerical data offers useful insights into the microstructure of the SS316L/IN625 FGM, which may be utilised to enhance its design and anticipate its performance in dedicated applications.

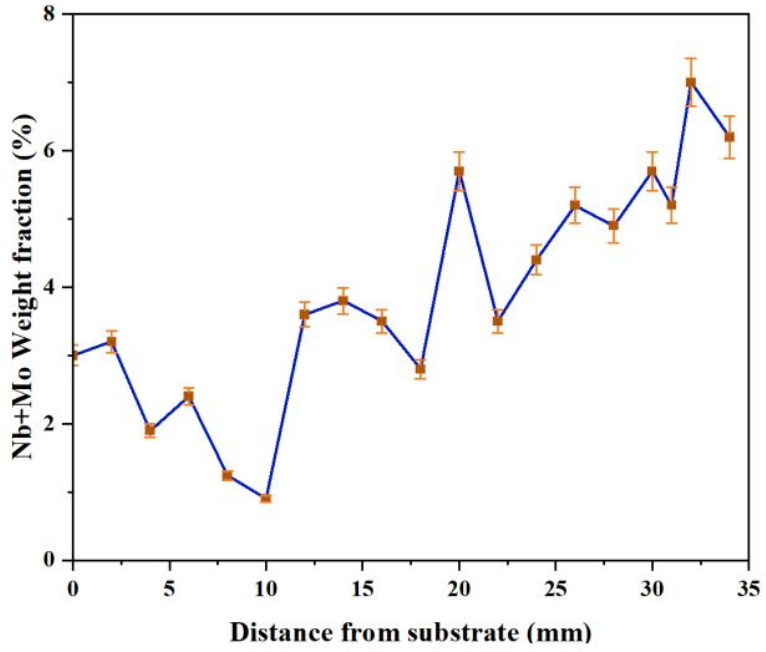

Fig. 4.7 Weight fraction of Nb + Mo along the gradient of CG-FGM sample

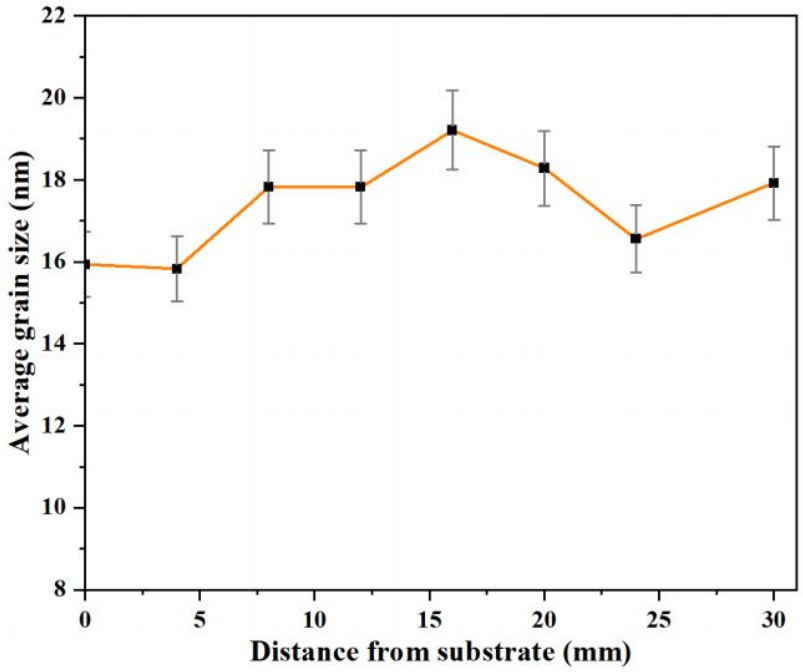

Fig. 4.8 Average grain size of SS316L/IN625 CG-FGM along the build direction.

4.5 Hardness analysis

Micro-indentation hardness was performed in order to study the mechanical behaviour of the build parts. It was tested on polished samples at 3 N load applied for a period of 18 sec (total time distribution) as 4–10–4 time zones, represented for loading, holding, and unloading time respectively. Multiple indentations along the build direction with 1 mm distance between successive indents were performed. Here, each hardness reading was the average outcome of three indents made in lateral direction. Fig. 4.9 shows the found hardness behaviour for both CG-FGM and SW-FGM.

In the case of CG-FGM a sudden spike was observed after the initial distance of ~2 mm. It could be because of the migration of Cr element due to multiple reheating. This migration is prominently visible in EDS mapping recorded and presented in Fig. 4.9a. Gradual increase in hardness from ~180 HV to ~230 HV was observed afterwards, as the composition of Ni increased. The hardness variation for SW-FGM was wavy and following the designed composition with varying peaks for IN625. These peaks were prominent and

distinct in the case of triple layer, compared to double and single layer alternate material deposition sample.

The fabricated FGMs yielded variation in hardness as designed and lies in the similar ranges as reported in the literature [19,53]. The conducted experimental research shows the potential of making different characteristics of FGM using multiple wire arc additive manufacturing process.

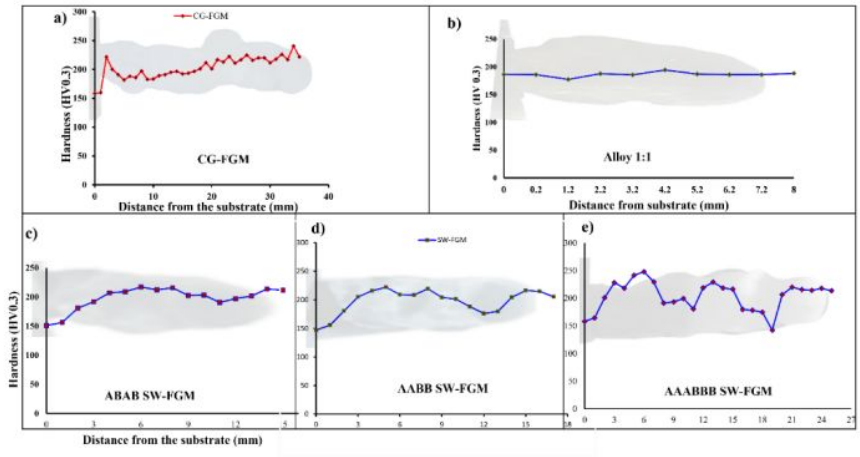

Fig. 4.9 Microhardness variation of (a) CG-FGM, (b) Alloy with 50% SS316L / 50% IN625 and (c), (d), (e) SW-FGMs from substrate to top (Error % =~5).

4.6. Tribological analysis

A linear reciprocating tribology test was performed utilising tungsten carbide (WC) of 0.5 mm diameter as counter body (spherical ball). The stroke length chosen was 3–6 mm along with 20 Hz frequency and 10 min time duration at 15 N dead normal load.

4.6.1. COF behavior of CG-FGM

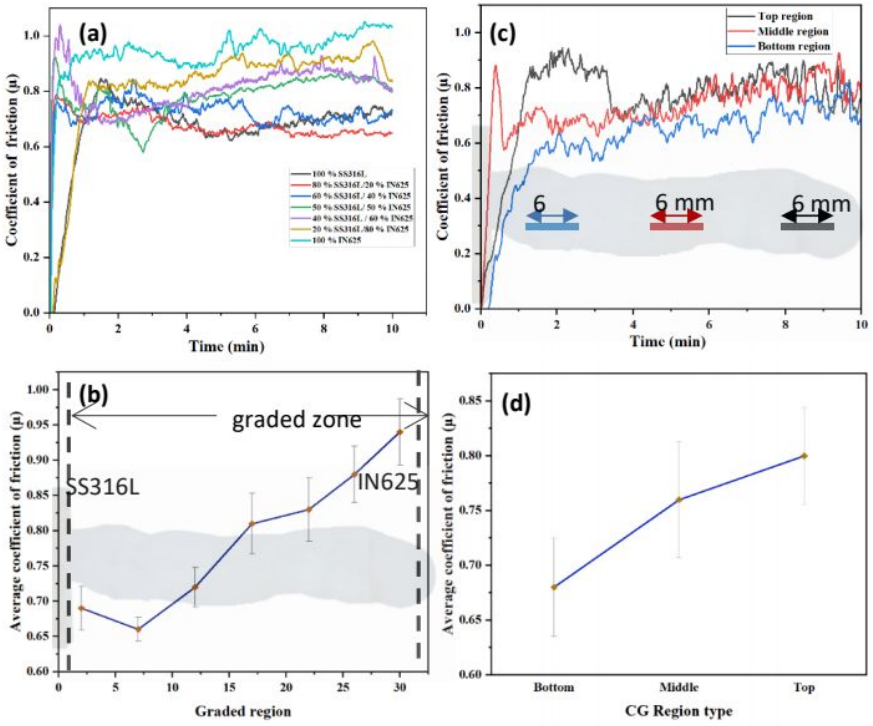

Fig. 4.10 (a), (b) Wear behaviour showing the coefficient of friction (μ) vs Time along the gradient in XY plane of deposited CG-FGM. (c), and (d) Wear characteristics at top, middle and top regions on the cut crossection surface in YZ plane of CG-FGM.

In the case of CG-FGM it was performed at different heights in XY and YZ both the planes to understand wear properties in constant and varying compositions, respectively. Fig. 4.10a and 4.10b depict the variation in coefficient of friction (CoF) and the average CoF for various wear tracks in the XY plane at different heights along the Z direction. The results show that the average CoF increased steadily along the build direction (Z-axis), from 0.69 to 0.94 corresponding to 100% SS316L and IN625, respectively.

Typically, SS316L shows less wear resistance compared to IN625 material [54]. Hence, the average CoF gradually increased along the direction of IN625 dominance, which was in accordance with the presented design and previous studies, as reported by Liang et al., (2010). Wear tests were also conducted in the YZ plane at the top, middle, and bottom regions for the CG-FGM and presented in Fig. 4.10c and ‘d’. Here the CoF follows the similar trend i.e. 0.68, 0.76, and 0.80 at the bottom, middle, and top regions,

respectively. The observed fluctuations with time could be attributed to the compositional variation along the stroke length, which caused the counter body to remove the material non-uniformly due to the difference in hardness. This inherent behaviour caused the CoF to vary along the YZ plane according to the design.

4.6.2. COF behavior of SW-FGMs

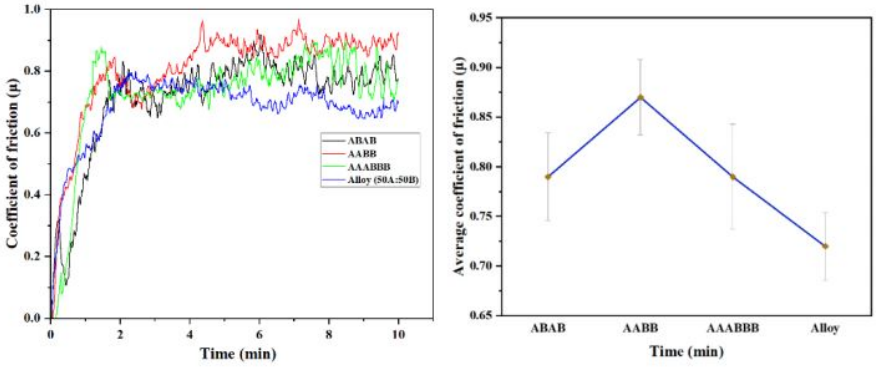

Fig. 4.11 Wear behaviour with friction coefficients of SW-FGMs of ABAB, AABB, Alloy (50A:50B) in YZ plane

Fig. 4.11 shows the obtained CoF and average CoF for SW-FGMs and alloy (50% A+50% B) with time. The average CoF obtained were 0.79, 0.87, 0.79 and 0.72 for ABAB, AABB, AAABBB and alloy, respectively. The ABAB and alloy showed similar values of the average CoF, with a slight difference of 0.07. It could be because of alloying effect of ABAB sample as confirmed in EDS area scan analysis. The samples AABB and AAABBB showed a considerable fluctuation in CoF with time, and their average CoF found was higher than the alloy. It could be due to cold welding phenomena resulting from the running-in stage under repeated sliding along the stroke length of varying composition, as observed and reported by Chen et al. (2020). This cold welding typically occurs between the counter body (ball) and the friction sample, as reported by Zhang et al., 2003 [55]. Since AABB and AAABBB have distinct regions of individual materials and transition zone, the CoF would depend largely on the location of the test. Therefore, it could be said that variation in CoF would depend on the number of layers of individual materials. In contrast, ABAB and the alloy, with minimal or no distinct regions of identifiable individual materials present along the stroke length,

exhibited low COF. This could be due to the gradual change of the abrasive wear mechanism from two to three contact surfaces in the absence of a running-in stage [56]. The SS316L dominating regions exhibited abrasive wear, which is characterised by the removal of material due to the sliding of hard particles or surfaces against the material surface. This type of wear is commonly caused due to the formation of grooves or scratches on the material surface. IN625 dominating regions exhibits a combination of abrasive and adhesive wear. Adhesive wear occurs when two surfaces in sliding contact adhere together and then rupture, resulting in material transfer and surface damage. IN625 is prone to galling and seizing in dry sliding conditions due to its low thermal conductivity and high ductility (Hartline, n.d.). In the transition regions, the wear mechanism was found to vary depending on the composition.

The wear mechanism observed in these regions was a combination of abrasive, adhesive, and fatigue wear. It also revealed greater wear damage compared to pure SS316L/IN625 regions. Fatigue wear is characterised by the progressive and localised damage to the material surface due to cyclic loading. The fatigue wear observed in the transition regions might be attributed to the formation of microcracks and voids, which act as stress concentrators and promote crack propagation. While the abrasive wear in this zone might be attributed to the presence of hard phases such as intermetallics.

4.6.3. Specific wear rate of CG-FGM

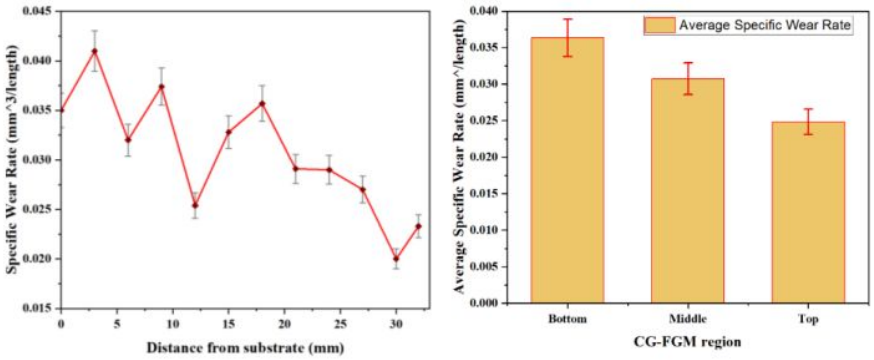

Fig. 4.12 Wear characteristics showing specific average volume removal of CG-FGM in the YZ plane.

The wear rate of CG-FGM measured through the profile obtained from the Profilm 3D along the YZ build direction was shown in Fig. 4.12. The volume removed per unit length decreased with the increase in distance from bottom to top. It could be due to, with the increase in IN625 content the secondary phases and running in stage makes the surface smooth and polished with time [57]. This result in a decrease in material removal rate with increase of IN625 content in regions compared to SS316L regions [58].

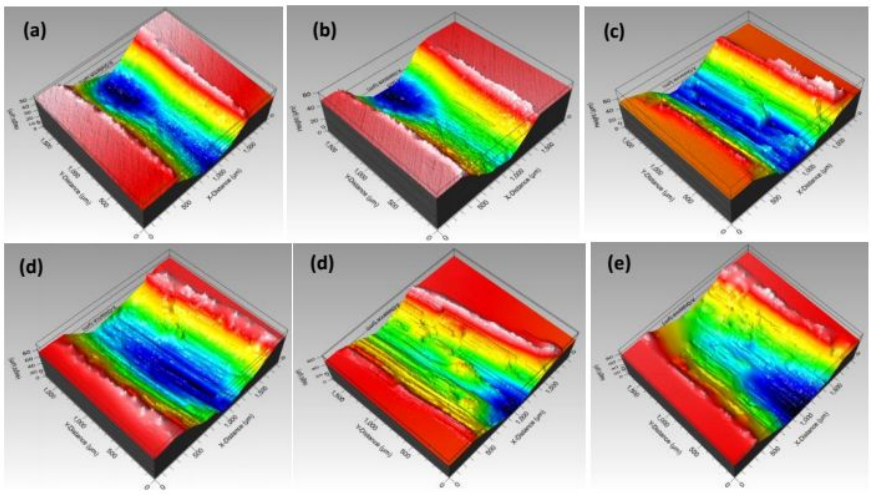

Fig. 4.13 Optical 3D profiles obtained at different regions of CG-FGM in YZ plane along Z direction from (a) top region to (f) bottom region.

The acquired profiles of CG-FGM at different locations obtained in the YZ plane is shown in Fig. 4.13. Wear track depth was higher in SS316L than IN625 regions. It could also be observed that the uniformity in wear rate in alloying regions as compared to less uniformity in dominating materials region.

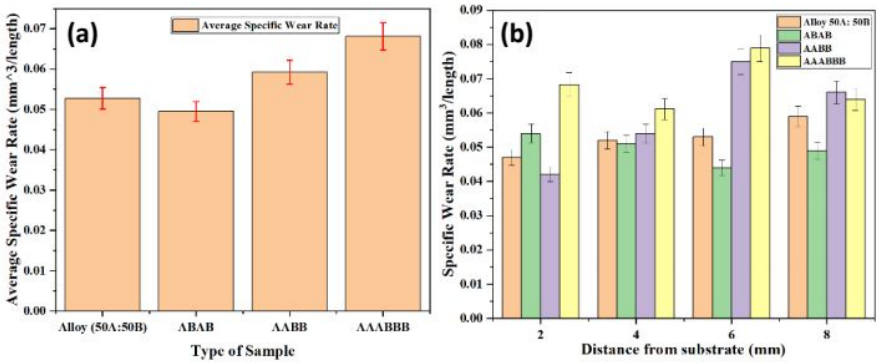

Fig. 4.14 Wear characteristics showing specific average wear rate and regional wear rate of Alloy (50 A:50 B), ABAB, AABB, and AAABBB SW-FGM samples in YZ plane.

4.6.4. Specific wear rate of SW-FGMs

Fig. 4.14 shows the specific volume removal for SW-FGMs in the YZ plane. The volume removed per unit length was measured from the wear profiles captured from Profilm 3D optical profilometer as shown in Fig 4.15. It is evident that the average volume removed increases with the increase in individual sandwich layered structures as shown in Fig 4.14. It could be due to the high running-in stage resulting from the composition fluctuation along the stroke length of higher sandwich layered structure [59]. This phenomenon could also be correlated with microhardness variation along the build direction. It can be understood from Fig.4.14b that over the distance from bottom to top, the volume removed also vary according to the compositional variation for SW-FGMs design. These distinct peak and valleys fluctuation can be seen more appropriate in the high sandwich layered structures. Meanwhile, the alloy and ABAB showed volume removal rate also as identical as the EDS and coefficient of friction analysis.

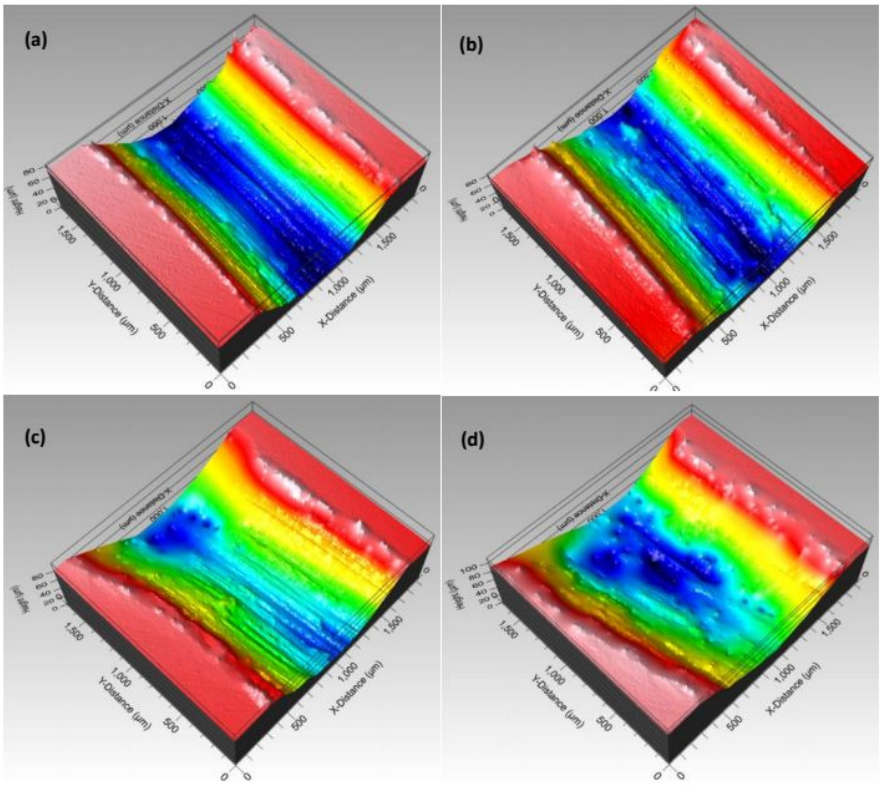

Fig. 4.15 Wear profiles showing depth and material removed for (a) Alloy (b) ABAB (c) AABB (d) AAABBB samples in YZ plane.

In conclusion, it could be said that the gradual transition of material composition in FGMs from SS316L to IN625 allows for a smooth variation of properties, resulting in improved performance and reduced wear. As observed in wear tests, the presence of IN625 in FGMs helps to decrease the wear rate at the desired locations. This makes IN625 a promising material for use in conjunction with SS316L in various applications where wear resistance is critical.

Chapter 5 RESULT AND DISCUSSION (Module 2)

5.1 Data Collection

5.1.1 Bead geometry

All the specimens were observed under an optical microscope to capture the cross-sectional profile of the deposited beads (Fig. 3.2). The geometrical features of the bead, i.e., the width and the height, were extracted from the obtained images and were used for further analysis (Table 1). It was observed that the alloy composition did not have any significant effect on the bead geometry. However, the travel speed and the arc current affected the bead geometry markedly. Fig. 5.1 demonstrates the effect of travel speed and current on bead width and height. Higher travel speed reduces both bead width and height, which was influenced by low material deposition rate, low line energy and high cooling rate during the deposition. The decision to maintain a constant wire feed speed (wfs) of 4 m/min resulted in a reduction in the material deposition rate. The lower line energy in the case of faster speed, limits the heat accumulation, resulting in rapid solidification and less material flow. Conversely, increasing current would boost the heat input, elevating molten material flow and bead width. However, the same would result in a reduced height. In summary, higher travel speed decreases both bead width and height, while increased current increases width and decreases height.

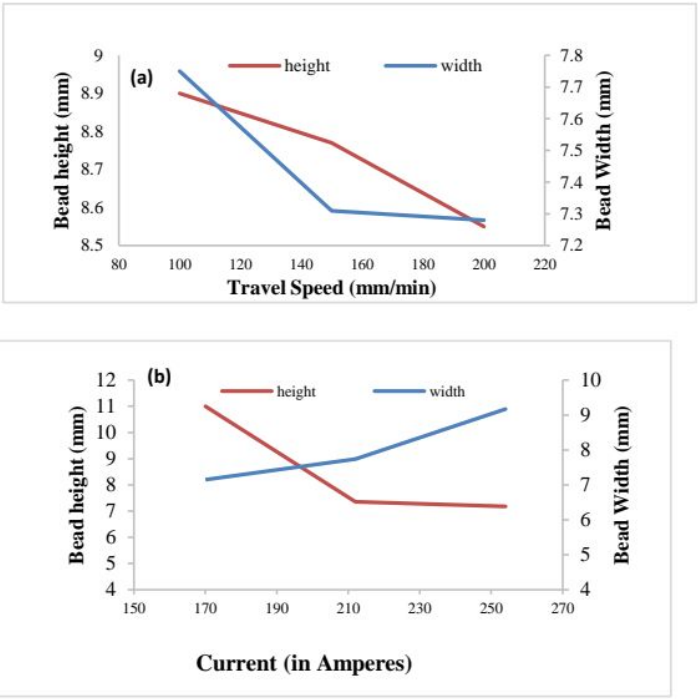

Fig. 5.1 Effect of (a) travel speed, (b) arc current on the bead geometrical properties, i.e., bead width and height.

5.1.2. Hardness

The hardness variation analysis on the selected three specimens with different SS316L/IN625 alloy compositions (3:1, 2:2, 1:3) was performed along the height. The variation is presented in Fig 5.2. The hardness remained almost the same for all three cases along the height. However, the average hardness was different for the three compositions. The trend showed that the increase in SS316L composition decreased the hardness, while the increase in IN625 content increased the hardness. The material with equal composition of SS316L/IN625 (1:1) showed the average hardness of the other two samples. This behaviour was observed due to the difference in the mechanical properties of the two alloys, i.e., SS316L and IN625. SS316L is a stainless-steel alloy with lower hardness compared to IN625, which is a nickel-based superalloy known for its high strength and hardness. Detailed analysis is discussed later.

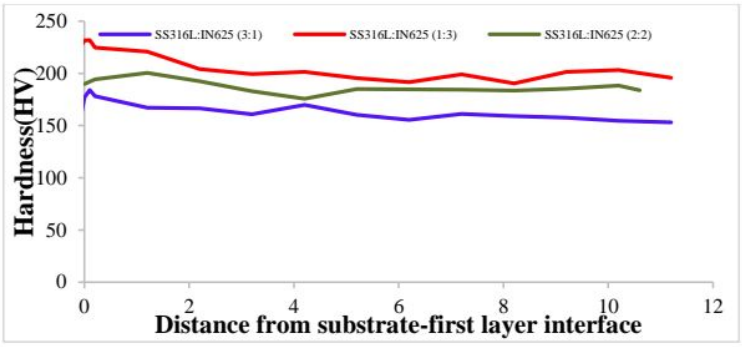

Fig. 5.2 Effect of composition on Hardness property taken along the build direction.

5.1.3. Tribological properties

5.1.3a Wear Characteristics

The wear test was conducted by subjecting the metallographically prepared surface of specimens to controlled conditions, evaluating its durability and resistance to wear and tear. A linear reciprocating wear tester was used with a tungsten carbide (WC) ball of 0.5 mm diameter as the counter body. The stroke length was 3-6 mm along with 20 Hz frequency and 10 min duration at 15 N dead normal load. Throughout the test, relevant data was diligently collected to assess crucial performance parameters, including coefficient of friction and frictional force. The wear rate was calculated using the measurement of volume loss. A 3D optical profilometer (Filmetrics, Profilm3D) was used to capture the wear profile and volume loss measurement.

The wear rate and coefficient of friction (COF) variation with respect to composition was studied and presented in Fig. 5.3. With the increase in composition from 1 (75% SS316L: 25 % IN625) to 3 (25 % SS316L: 75% IN625) the Specific wear rate was increasing, while COF showed a decreasing trend. The wear rate decreases as the composition shifts towards a higher proportion of IN625, known for wear resistance. Increased IN625 led to a more wear-resistant surface, reducing material loss. However, the COF increased as the IN625 percentage rose, possibly due to increased adhesion. These findings align with the literature on wear-resistant alloys and their effects on wear rate and COF [57].

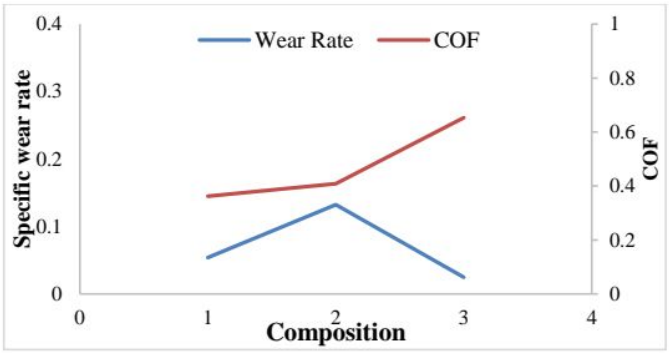

Fig. 5.3 Effect of composition on Specific Wear Rate and Coefficient Of Friction (COF).

5.1.3b Fracture toughness and Scratch hardness

The scratch test was performed to calculate the scratch hardness and the material's fracture toughness. The test involved subjecting the material to controlled scratching using a standardised (ducom TR–101). The force applied during the scratch test was measured, and the resulting scratch was examined and analysed. By studying the dimensions and characteristics of the scratch, along with the applied force, scratch hardness and fracture toughness were calculated using the Eqn 1 and 2, respectively. It allowed for a quantitative evaluation of the material's ability to withstand crack propagation and fracture under applied loads. Through this meticulous approach, valuable insights could be gained into the material's strength and durability, enabling informed decisions in various engineering and manufacturing applications.

$$\text{Scratch hardness (Hs)} = \frac{8F_N}{\pi b^2} \qquad \text{eq (1)}$$

Where F_N is applied normal load, and b is the scratch track width

$$\text{Horizontal force } (F_T) = 2C\,\frac{[sin\theta]^{1/2}}{cos\theta} K_c d^{1/2} \qquad \text{eq (2)}$$

Where p is the perimeter, F_T is horizontal force, and A is the horizontal projected load-bearing contact area, K_c fracture toughness, and d is the penetration depth

Fig. 5.4 shows the effect of composition on fracture toughness and scratch hardness. The variation in composition caused variation in fracture toughness

and scratch hardness. The direct relationship was caused by an increase in the composition of the IN625 in the alloy resulting in a higher concentration of strengthening elements, such as Ni, Mo, and Nb or impurities. These elements contribute to the formation of a stronger and more durable microstructure within the alloy, thereby enhancing both fracture toughness and scratch hardness.

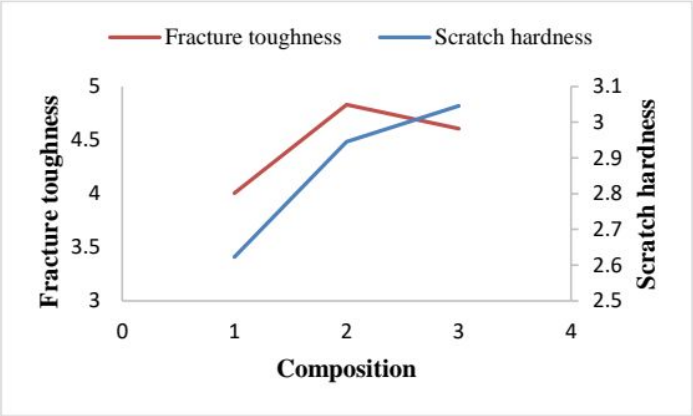

Fig. 5.4 Effect of Composition on Fracture toughness and Scratch hardness properties

5.1.4. EDS Area Scan Analysis

EDS area scan was performed along the build direction to validate the actual composition through major governing elements, i.e., Fe and Ni. An area of 0.5x0.5 mm^2 at three locations, as top, middle and bottom regions, was scanned, and the composition of Fe and Ni was averaged. Fig. 5.5 shows the Fe/Ni composition of SS316L/IN625 alloys for various composition ratios (1–3), current (170–254 A), and speed (100–200 mm/min). It was found that the Fe, Ni, and other elements' content varied majorly with respect to the composition ratio. These results are in accordance with the designed experiments validating the effectiveness of the WAAM-TIG process to deposit alloys with reliable accuracy. The tailored composition of the alloys could be used to meet specific application requirements, such as corrosion resistance, strength, and durability.

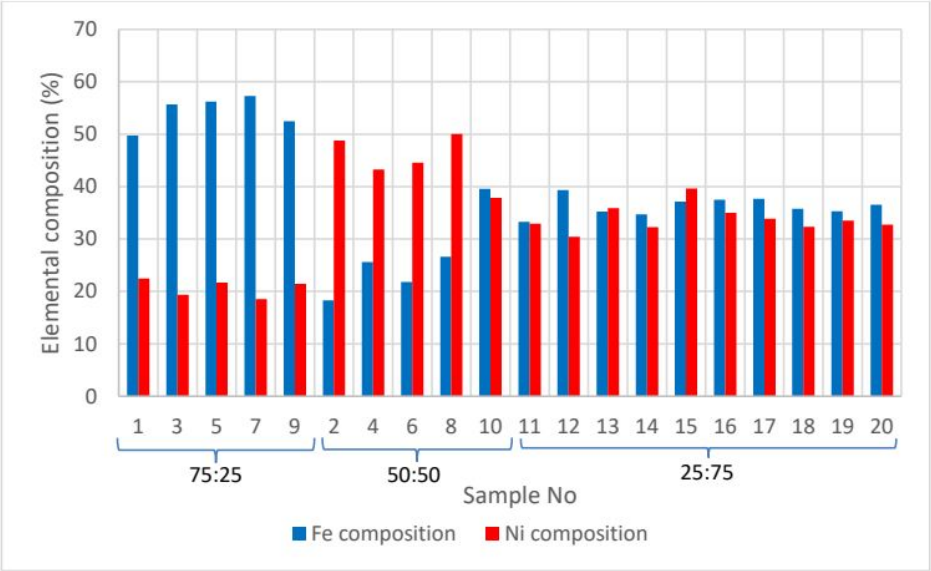

Fig. 5.5 EDS elemental composition distribution of SS316L/IN625 CCD design of experiments

5.2 Statistical Analysis discussion

5.2.1 Response analysis (individual effects of input factors)

Table 1 shows the outcomes of the experiment's 20 runs with measured geometrical and mechanical properties for each run. The composition was found to be an important factor during the procedure. ANOVA was performed to measure the variability and significance of the effects of factors on response variables. The *normal plots of the standardised effects* in Fig. 5.6a,c,e,g,i,k and m, and *residual vs observation order plots* in Fig. 5.6b,d,f,h,j,l, and n for response variables shows relation behaviours. These suggest that the models used in the analysis do not violate the assumptions of residual normality (the residuals follow a normal distribution) and independence (the residuals are not correlated with the observation order).

A *residual versus order plot* is used to test whether residuals are independent of each other. If the residuals are independent, there should be no patterns or trends when displayed in time order. However, if the points show patterns, it suggests that the residuals may be correlated and not independent and are influenced by some unknown factors, violating the independence assumption. The plot should ideally show residuals randomly distributed around the centre

line, where the difference between the observed values (Y_i) and the fitted model response ($\hat{y}_i$) is a residual, represented in equation (8). The inclined line in the normal plot would indicate the expected pattern of the standardised effects if they were normally distributed. It represents the relationship between the standardised effects and the cumulative probabilities associated with a standard normal distribution. The normal plot is a visual tool to assess the departure from normality and identify potentially influential factors. In summary, less deviation from the inclined line typically indicates that the factor is not statistically significant. In contrast, a larger deviation suggests that the factor significantly impacts the response variable. However, the final determination of significance should be based on appropriate statistical tests.

$$E_i = Y_i - \hat{y}_i \tag{8}$$

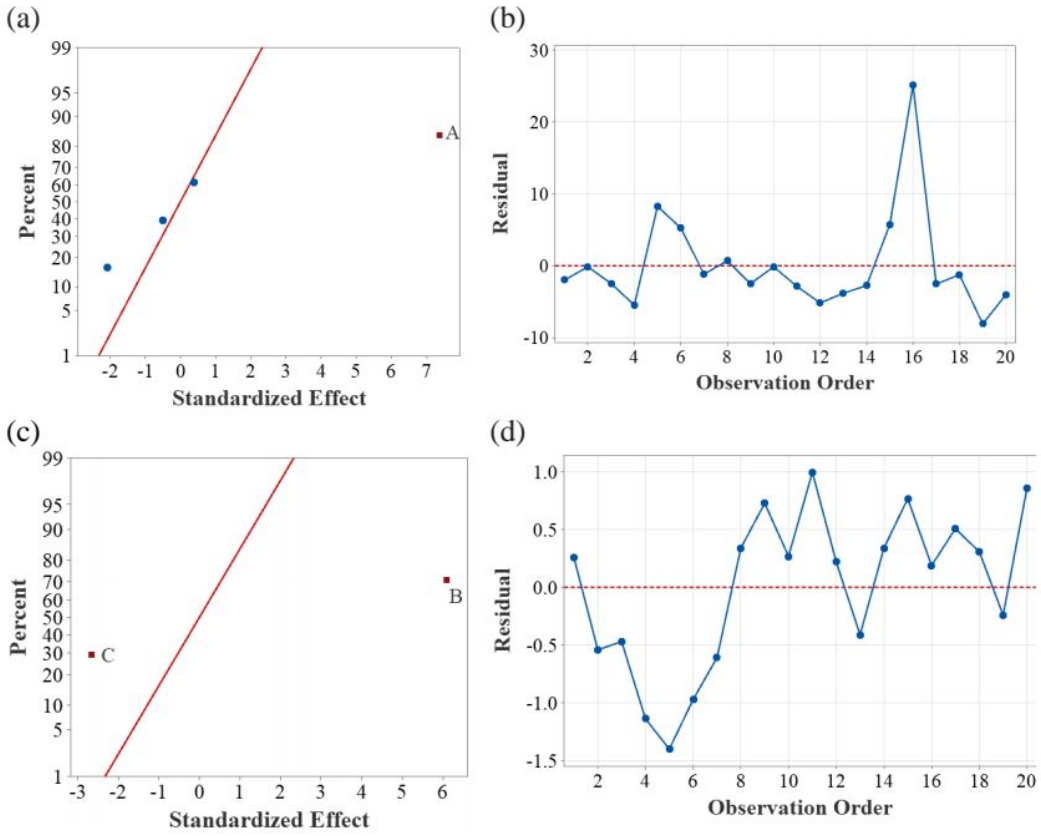

(e)

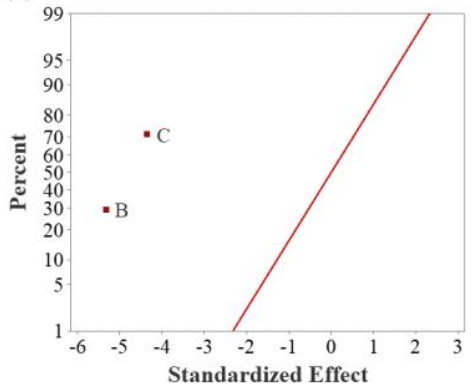
Percent
Standardized Effect
C
B

(f)

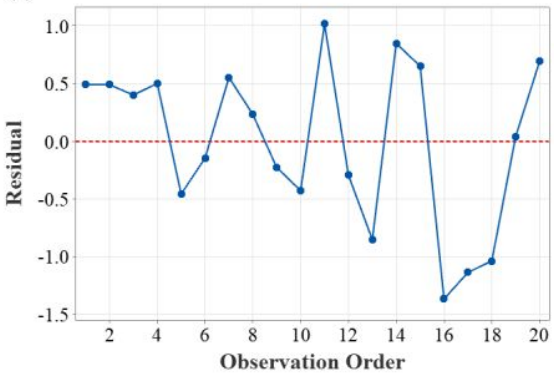
Residual
Observation Order

(g)

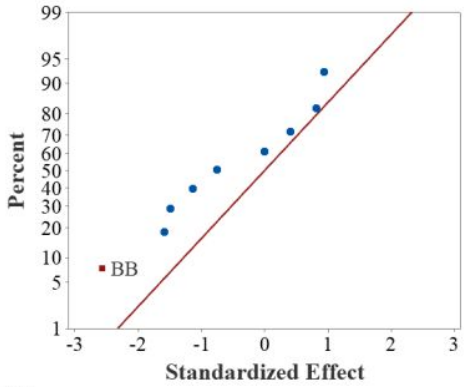
Percent
Standardized Effect
BB

(h)

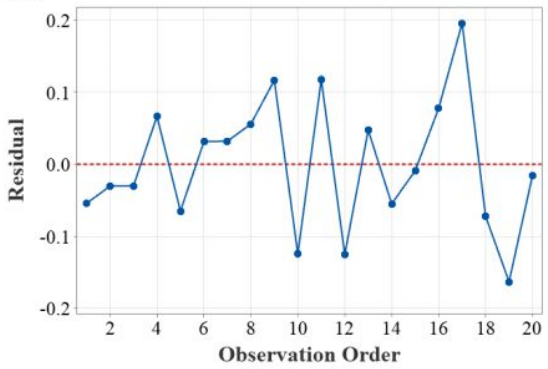
Residual
Observation Order

(i)

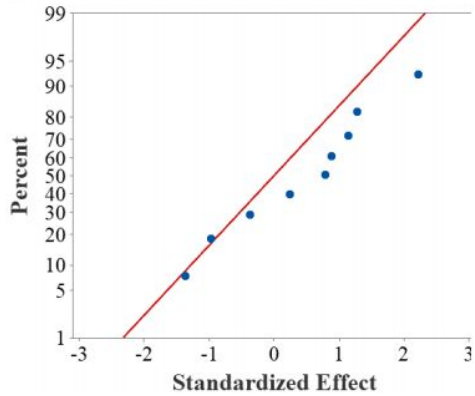
Percent
Standardized Effect

(j)

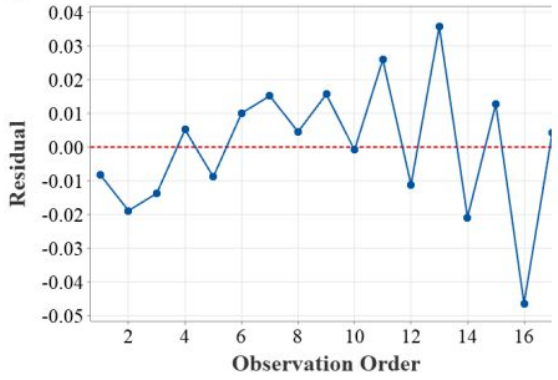
Residual
Observation Order

(k)

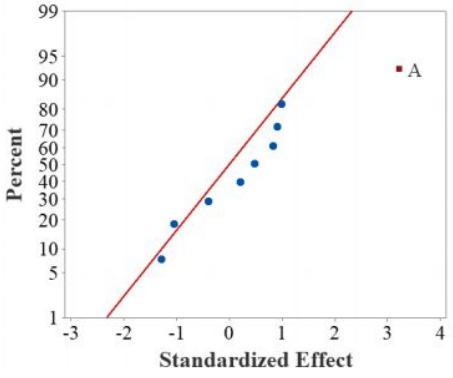
Percent
Standardized Effect
A

(l)

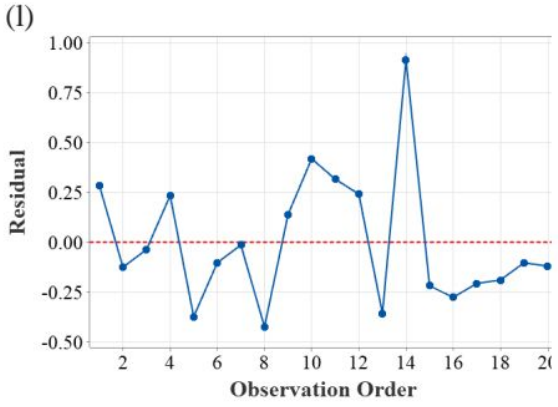
Residual
Observation Order

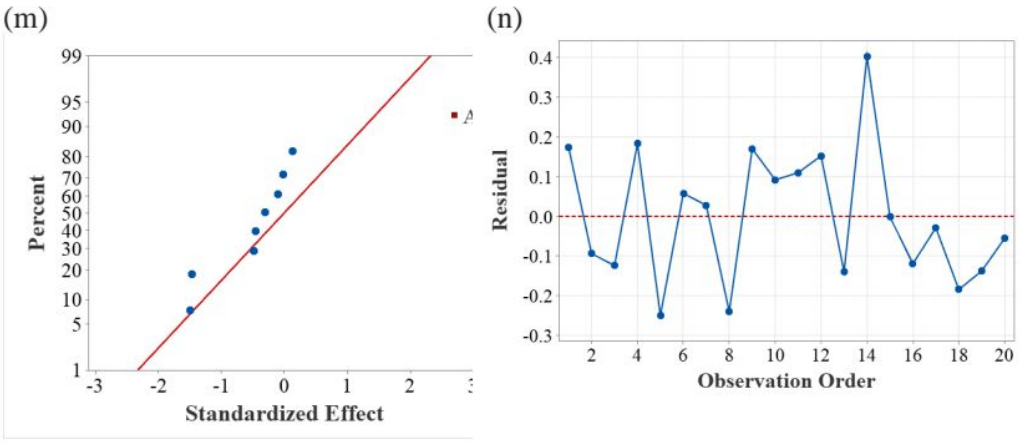

Fig. 5.6. Normal residuals probability and Residuals vs observation order plots respectively for responses (a), (b) hardness, (c), (d) Bead width, (e), (f) Bead height (g), (h) COF (i), (j) Wear rate (WRR), (k), (l) Fracture toughness and (m), (n) Scratch hardness.

ANOVA begins with the premise that the input parameters have no substantial impact on the output, termed as null hypothesis [25]. F-statistic is measured by examining the means of various groups to interpret whether the output varies widely when the input is altered. If the F-statistic is adequate, it may be concluded that there is a strong correlation between the input and output [16].

If the F-statistic exceeds the threshold F-statistic in the F distribution table, it means that the variability of the response variablesfor different input variables is significant. It allowed to confidently conclude that the input variable significantly impacts the output parameter. The p-value is the likelihood of null hypothesis acceptance, which claims that the mean value of the response variables corresponds to various input factors being the same. If the p-value is less than the desired significance level, which is usually 0.05, in that case, the null hypothesis is rejected, and it is possible to conclude that the response variables' mean value was significantly different for various input factors [60]. Rejecting the null hypothesis means accepting the alternative hypothesis, which states that the effect of that variable on response is significant. In statistics, degrees of freedom refer to the number of independent information available in a sample or a statistical model. i.e., the number of observations in a sample that are free to vary. Higher Adj MS values suggest greater variability or larger mean square differences, indicating a potentially more significant effect.

5.2.2 Individual response analysis

5.2.2a Hardness response analysis

Fig. 5.7 illustrates the influence of parameters, i.e., composition, current and travel speed, on the hardness. The hardness values ranged from 160 HV at composition-1 (75: 25) to 200 HV at composition-3 (25:75). The hardness increased with the increase in IN625 content in the material. The trend in hardness property in this study observed was consistent with the literature findings available [13]. This behaviour was due to the higher hardness of pure IN625 (~220 HV) than SS316L (~150 HV) material. At composition-2 (50: 50), hardness was found to be in the range of 185–195 HV. Fig. 5.7a indicates that composition is the only parameter significantly impacting micro-hardness response. The F-statistic for composition was greater than that for current and travel speed, indicating the major contribution to hardness response. ANOVA for the interaction between composition, current and travel speed was conducted, and the current and travel speed were found to contribute insignificantly, as shown in Table 6. It was also observed from the Pareto chart in Fig. 5.7b that only composition was higher than the threshold detected by a 95% confidence interval (red dotted line), with current and speed. The x-axis shows the variation from the general mean for each process parameter. Here, a larger deviation suggested that the individual parameter affects the response value more.

Table 6 ANOVA (analysis of variance) results of composition, current and speed for hardness response

Source	DOF	Adj-SS (degree^2)	Adj-MS (degree^2)	F-value	P-value
Composition	4	3440.7	935.9	54.24	0.0002
Current	1	16.6	16.7	4.38	0.821
Speed	1	8.7	8.6	3.41	0.615

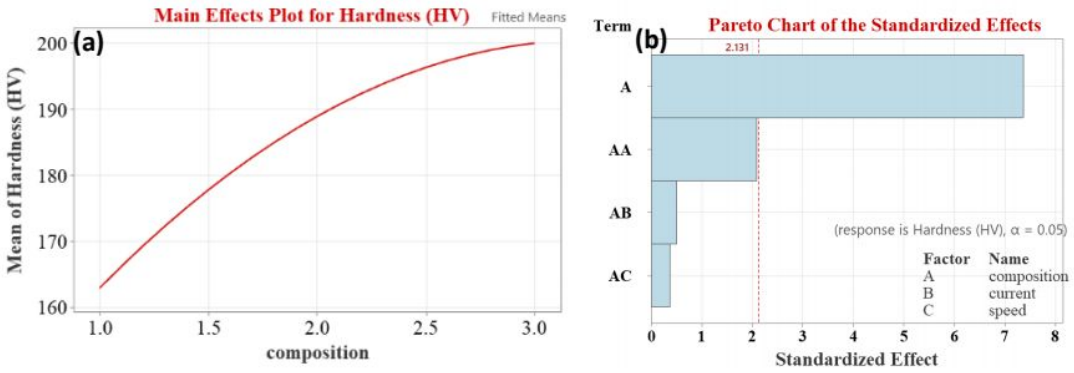

Fig. 5.7 (a) Individual effect of composition, current and travel speed on mean hardness.and (b) Pareto chart showing standardised effect of composition, current, speed and their interactions on hardness.

5.2.2b Bead width

Deposited bead size showed a wide variation when the current was altered from 170 A to 254 A. However, the bead feature variation was negligible for the composition parameter as input. Fig. 5.8 illustrates the effect of parameters, i.e., composition, current and travel speed, on the bead width feature. Current and travel speeds had similar but opposite effects on the bead width. In terms of energy, the higher the current, the higher the energy generated. Higher input energy would produce a bigger melt pool, melting the previously solidified layers. ANOVA (Table 7) performed for the current and speed had a p-value of 0.0001 and 0.0002, respectively, showing a considerable effect on the bead geometry. In contrast to the hardness response, the current and travel speed showed an effect on bead geometry. The bead width increased from 6 mm to 9 mm at the current, increasing from 170 A to 254 A. Also, the bead width decreased from 8 mm to 6.8 mm at the travel speed, increasing from 100 A to 200 A.

Fig 5.8a indicates that current and speed are the parameters that showed the major effect on bead width output. The F-statistic for current and speed are greater than the composition parameter, indicating a great contribution to bead width response. This behaviour is due to the high current leading to more heat generation and causing the material to melt and flow outwards, resulting in a higher bead width.

Table 7 Analysis of variance (ANOVA) results of composition, current and speed for bead width response.

Source	DOF	Adj-SS (degree^2)	Adj-MS (degree^2)	F-value	P-value
Composition	1	0.47	0.45	1.49	0.346
Current	2	19.57	19.572	89.85	0.0001
Speed	2	3.72	3.72	17.08	0.0002

From the Pareto chart in Fig 5.8, it was observed that only current and travel speed parameters had higher values, more than 0.95 of threshold (95 % confidence interval). However, current was the main factor contributing to the bead width model. The x-axis shows the difference of each process parameter from the mean value. The larger the value, the greater the effect on bead width output.

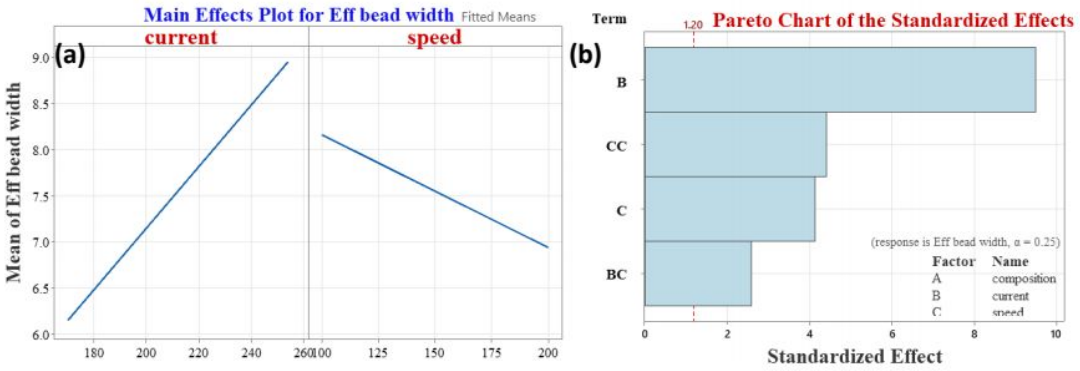

Fig. 5.8 (a), dividual effect of compostion, current and travel speed on mean/average bead width. and (b) Pareto chart showing standardised effect of composition, current, speed and their interactions on bead width response.

5.2.2c Bead height

In Fig. 5.9, the effect of parameters i.e., composition, current and travel speed on the bead height factor is illustrated. The higher the current or travel speed, the greater the bead height of the melt pool altered in the span of 7.5 to 10 mm. Due to high current, heat generation increases, resulting in more spreading of molten metal due to extreme temperature and low cooling rate.

The bead height decreased from 10 mm to 7.5 mm at the current, increasing from 170 A to 254 A. Also, the bead height decreased in similar range from 10 mm to 7.5 mm at the travel speed, increasing from 100 A to 200 A. The bead height decreased with the increase in current and travel speed during the process. Figure 5.9a indicates that current and speed are the parameters showing major effect on bead width output. The F-value for current and speed were greater than the composition parameter, indicating a significant contribution to bead height response.

Table 8 Analysis of variance (ANOVA) results of composition, current and speed for bead height response

Source	DOF	Adj SS (degree2)	Adj MS (degree2)	F-value	P-value
Composition	1	1.574	1.573	0.36	0.925
Current	2	26.27	13.135	32.04	0.0001
Speed	2	15.75	10.5268	21.42	0.0001

It was also observed from the Pareto chart analysis (Fig. 5.9b). The composition didn't show any significant value and was below the threshold level. The composition was ignored while optimising the process to obtain excellent and controlled bead height under the formed melt pool

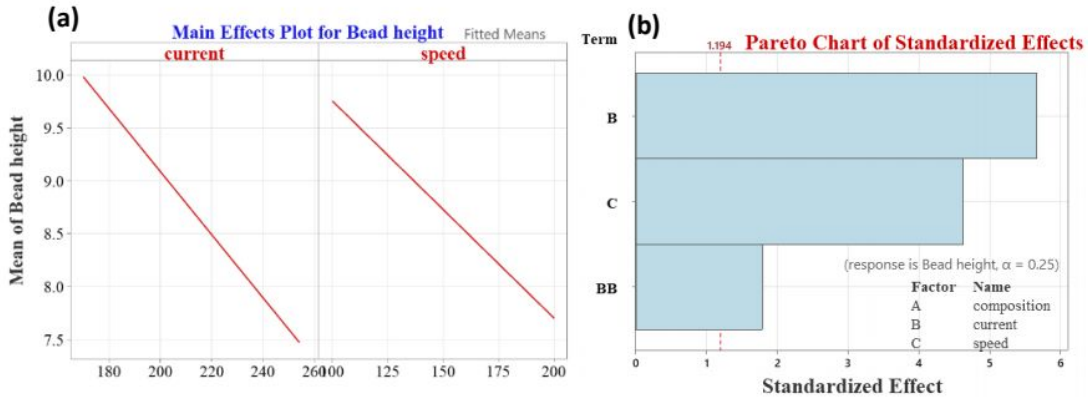

Fig. 5.9 (a) Individual effect of composition, current and travel speed on mean/average bead height and (b). Pareto chart showing standardised effect of composition, current, speed and their interactions on bead height response.

5.2.2d Fracture toughness and Scratch hardness

The scratch hardness and fracture toughness values are in line with the literature available for the similar material [61]. The effect of composition on fracture toughness and scratch hardness followed an increasing trend. The effect of travel speed on fracture toughness followed first increasing and then decreasing trend, and in the case of scratch hardness, it decreased throughout. While the effect of current showed an opposite trend between fracture toughness and scratch hardness, as observed in Fig. 5.10b, c. The fracture toughness was maximum for high current and composition with medium speeds. However, scratch hardness was maximum for high composition and speed with extreme currents. The composition, crystal structure, manufacturing processes, and microstructure of the material impact mechanical properties, such as fracture toughness and scratch hardness. The changes in the composition of SS316L and IN625 alloys can result in grain size and distribution variations, which alter the material's toughness and hardness.

ANOVA analysis showed the p-values (probabilistic value) for composition, current and speed as 0.023,0.98, and 0.66 in the scratch hardness model as represented in Table. 10, whereas 0.009, 0.429, and 0.854, respectively, for fracture toughness shown in Table. 9. The combined effect of composition and speed majorly contributed to the fracture toughness and scratch hardness models. The fracture toughness values lay in the 3.3 to 5.7 Mpa √m range, whereas scratch hardness values lay in the 2.3 to 3.4 GPa range.

$$F_T \propto 2\,\frac{[\sin\theta]^{\frac{1}{2}}}{\cos\theta} K_c\, d^{3/2}$$

Where d is the penetration depth in mm, K_c is Fracture toughness in Mpa $m^{1/2}$, θ is half-apex angle in degrees, and F_T is the applied force in N.

Table 9 Analysis of variance (ANOVA) results of composition, current and speed for Fracture toughness response

Source	DOF	Adj-SS (degree2)	Adj-MS (degree2)	F-value	P-value
Composition	1	2.095	2.241	10.37	0.009
Current	1	0.137	0.172	0.68	0.429
Speed	1	0.008	0.01	0.04	0.844

Table 10 Analysis of variance (ANOVA) results of composition, current and speed for Scratch hardness response.

Source	DOF	Adj-SS (degree2)	Adj-MS (degree2)	F-value	P-value
Composition	1	0.391	0.41	7.25	0.023
Current	1	0.00004	0.00003	0.0001	0.98
Speed	1	0.012	0.025	0.21	0.66

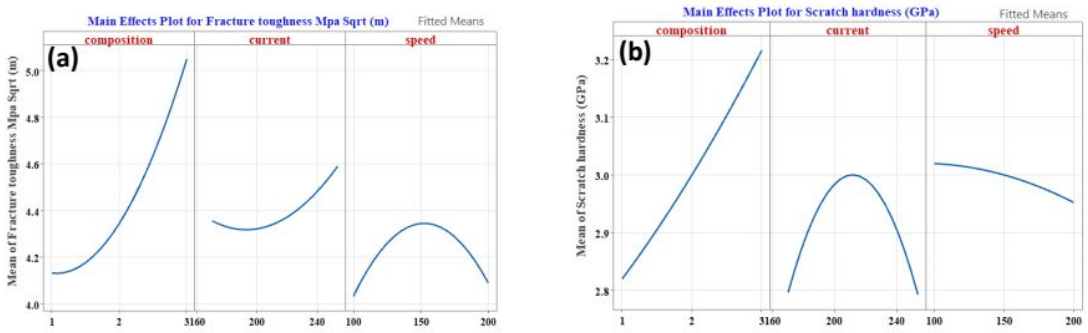

Fig. 5.10 Individual effect of composition, current and travel speed on mean/average (b) Fracture toughness and (c) Scratch hardness.

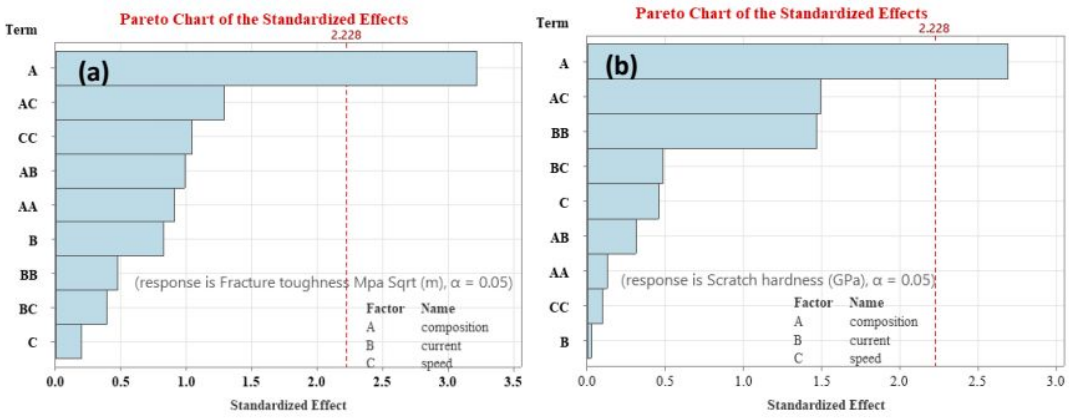

Fig. 5.11 Pareto chart showing standardised effect of composition, current, speed and their interactions on (a) Fractur toughness and (b) Scratch hardness responses.

Fig. 5.11 shows the Pareto chart, and it was observed that only composition exhibits a higher value than the threshold (red line representation). The higher the composition, the greater would be the fracture toughness values. Similar behaviour can be found in the scratch hardness model.

5.2.2e COF and Specific wear rate

The COF (Fig. 5.12) and specific wear rate (Fig. 5.13) were obtained by performing the reciprocating wear test on the specimens designed. The effect of composition and travel speed was higher in the case of COF. The greater the IN625 composition, the more would be the COF, whereas the higher the travel speed, the less would be the COF. The COF varied in the range of 0.3 to 0.93, with high COF ranges for IN625-dominated and low COF ranges for SS316L-dominated regions. The specific wear rate was dependent more on composition and input current. However, the specific wear rate first increased and then decreased with respect to composition, with a maximum at approximately 50:50 SS316L/IN625. The wear rate lay in the range of 0.03 to 0.2 mm^3. It represented that the COF and specific wear rate models showed an opposite trend with respect to composition. The literature suggests that SS316L-dominated regions show abrasive wear due to sliding hard particles or surfaces against the material surface, resulting in grooves or scratches. While IN625-dominated specimens show a combination of abrasive and adhesive wear due to low thermal conductivity and high ductility, making them prone to galling and seizing in

dry sliding conditions. The 50:50 SS316L/IN625 regions showed a combination of abrasive, adhesive, and fatigue wear with more significant damage than pure SS316L/IN625 regions. Fatigue wear might be attributed to the formation of microcracks and voids, while abrasive wear might be due to the presence of hard phases such as intermetallic.

Table 11 Analysis of variance (ANOVA) results of composition, current and speed for COF response.

Source	**DOF**	**Adj-SS (degree2)**	**Adj-MS (degree2)**	**F-value**	**P-value**
Composition	1	0.02	0.022	0.16	0.006
Current	1	0.0001	0..0001	0.01	0.9
Speed	1	0.0090	0.0069	0.57	0.47

Table 12 Analysis of variance (ANOVA) results of composition, current and speed for Specific Wear Rate response.

Source	DOF	Adj-SS (degree2)	Adj-MS (degree2)	F-value	P-value
Composition	1	0.0015	0.0014	1.62	0.001
Current	1	0.0043	0..0044	4.93	0.062
Speed	1	0.0061	0.0005	0.61	0.459

ANOVA analysis showed the p-values (probabilistic value) for composition, current and speed as 0.006,0.9, and 0.47 in the COF model, whereas 0.001, 0.062, and 0.459, respectively, for specific wear rate as represented in Table. 11 and 12. The combined effect of composition and current majorly contributed to the COF and specific wear rate models. The COF values lay in the range of 0.3 to 0.93, whereas specific wear rate values lay in 0.02 to 0.15 mm^3/mm.

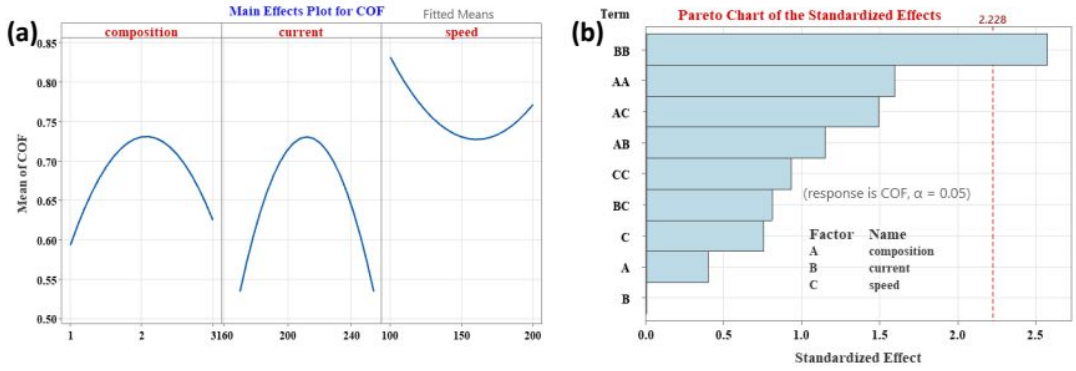

Fig. 5.12 (a) Individual effect of composition, current and travel speed on mean/average COF and (b). Pareto chart showing standardised effect of composition, current, speed and their interactions on COF response.

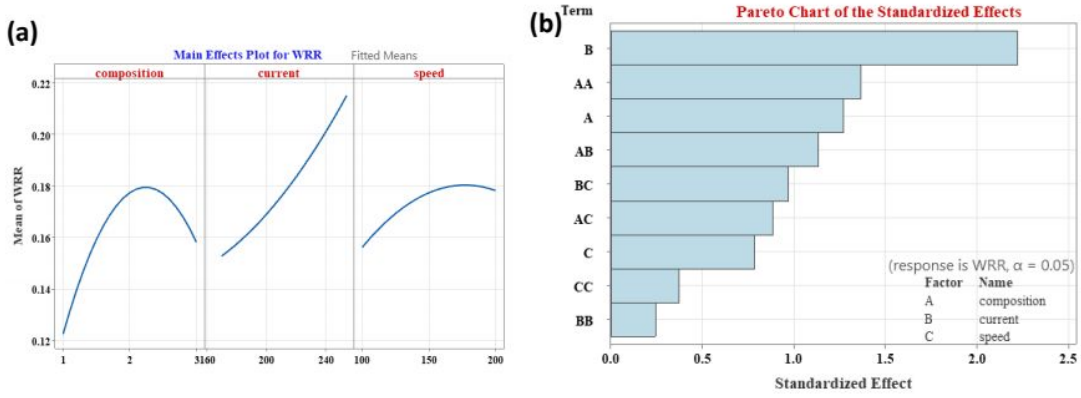

Fig. 5.13 (a) Individual effect of composition, current and travel speed on mean/average specific WRR and (b). Pareto chart showing standardised effect of composition, current, speed and their interactions on specific wear rate response.

5.2.3 Regression model analysis

The regression models for all the responses for various deposited bead characteristics are shown in Table 13. It is a powerful tool as it can forecast the output data based on the input levels of composition, current and travel speed. The model developed a regression equation for all responses with an R^2 value between 0.65 - 0.9%. This explains the strong relationship between the input factors and responses. These models can be employed to experiment with process parameters to calculate the optimal R^2 value for each output parameter. Higher R^2 values signify better fit, implying stronger relationships between factors and response. It helps evaluate model goodness of fit and predictability.

Table 13 Prediction of deposited bead responses using regression model. The nomenclature for composition, current and speed are considered as C, I, and S respectively.

Responses	**Model's Regression Equation**	**R^2**
Hardness (HV.)	188.96 + 18.55 C - 7.46 C*C - 1.45 C*I + 1.04 C*I	0.76
Bead width (mm)	0.97 + 0.0027 I + 0.0552 S -0.000369 S*S + 0.000204 I*S	0.89
Bead height (mm)	32.15 - 0.1647 I - 0.02052 S + 0.000318 I*I	0.78
Fracture Toughness	3.85 - 0.70 C - 0.0310 I + 0.0491 S + 0.245 C*C + 0.000073 I*I- 0.000113 S*S + 0.00373 C*I - 0.00410 C*S - 0.000030 I*S	0.608
Scratch hardness	-4.16 + 0.623 C + 0.0533 I + 0.0099 S + 0.018 C*CC - 0.000116 I*I- 0.000006 S*S - 0.00061 C*I - 0.00245 C*S - 0.000019 I*S	0.612
Coefficient-of friction	-4.42 + 0.959 C + 0.0470 I - 0.0101 S - 0.1213 C*C - 0.000111 I*I + 0.000028 S*S- 0.00122 C*I - 0.001329 C*S + 0.000017 I*S	0.703
Specific wear rate (mm^3/length)	-0.059 + 0.0230 C - 0.00040 I + 0.00162 S - 0.0247 C*C+0.000003 I*I-0.000003 S*S + 0.000283 C*I + 0.000186 C*S - 0.000005 I*S	0.658

5.2.4 Surface plots of models

The correlation between the response and factors was portrayed through surface plots and are presented in Fig 5.14. The correlation in all the models was non-linear, with little or much variation in response to the tuning of input variables. The areas of high and low response were evident due to the reverse effect of the input variable combination on the final response. The interaction effects might also be present between the factors (input variables). It might occur due to the relationship between one factor and the response variable depending on the values of another factor. An indication of an interaction effect can be observed through sudden changes in the

slope or shape of the plotted areas. The model is a good fit if the surface plot closely matches the actual data points.

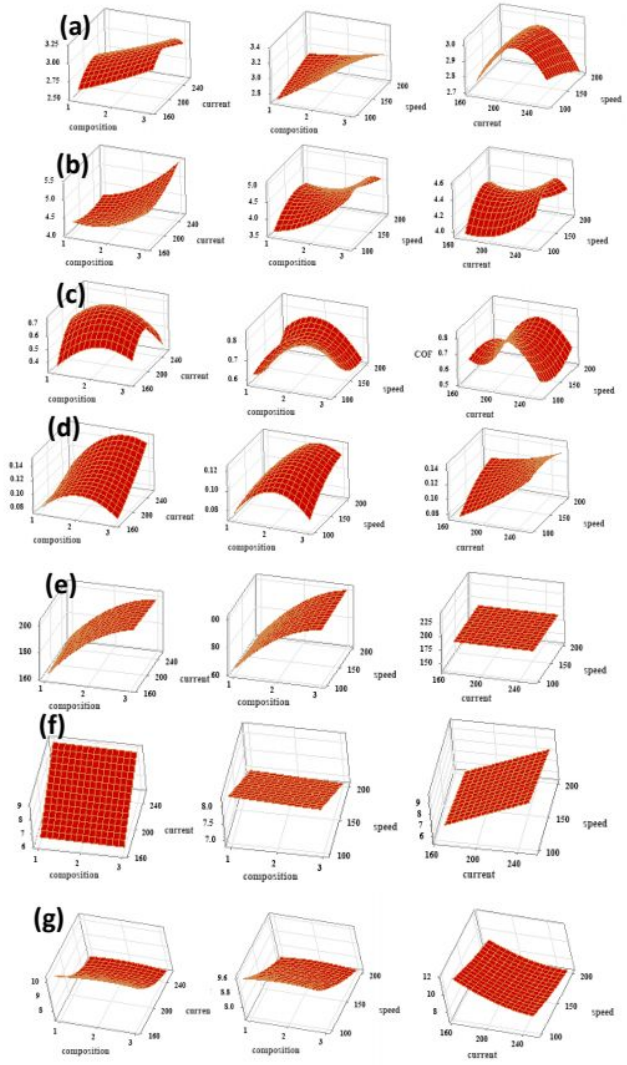

Fig. 5.14 Surface plots corresponding to composition, current and speed of models developed i.e., (a). Scratch hardness, (b) Fracture toughness, (c) Coefficient of friction, (d) Specific Wear Rate, (e) Hardness, (f) Bead width, (g) Bead height.

5.2.5. Multi-response optimisation and analysis

In the manufacturing of the SS316L/IN625 alloy using WAAM-TIG, several specific requirements are aimed for. These include achieving maximum hardness and fracture toughness and minimizing the wear rate. Apart from this, bead width and height of 6mm x 6mm was chosen for multi-response optimisation.

By attaining maximum hardness, the alloy becomes more resistant to deformation and wear, ensuring its durability and longevity. Similarly, high fracture toughness is essential as it enhances the alloy's ability to withstand cracks and fractures, ensuring structural integrity. Minimizing the wear rate is crucial to prolong the lifespan of the alloy and reduce material loss during usage. The specific bead width and height of 6mm x 6mm are chosen to ensure consistency and accuracy in the additive manufacturing process, resulting in uniform and reliable alloy structures. By meeting these requirements, the SS316L/IN625 alloy manufactured through additive manufacturing can deliver exceptional performance, durability, and reliability in various applications.

The composite desirability function can achieve multiple response objectives/goals. Figure 16 displays the optimal results with a composite desirability limit to address the multiple objective output response by pulling out the higher and lower point from the 3D surface plot concerning the defined objective. The optimum condition obtained was composition of 3 (3:1), current of 205 A, and voltage of 200 mm/min. The predicted values of hardness, specific wear rate, fracture toughness, bead width and height are 205 HV, 0.0904 mm^3/mm, 4.56, 7.60 mm and6.52 mm respectively with composite desirability of 0.63.

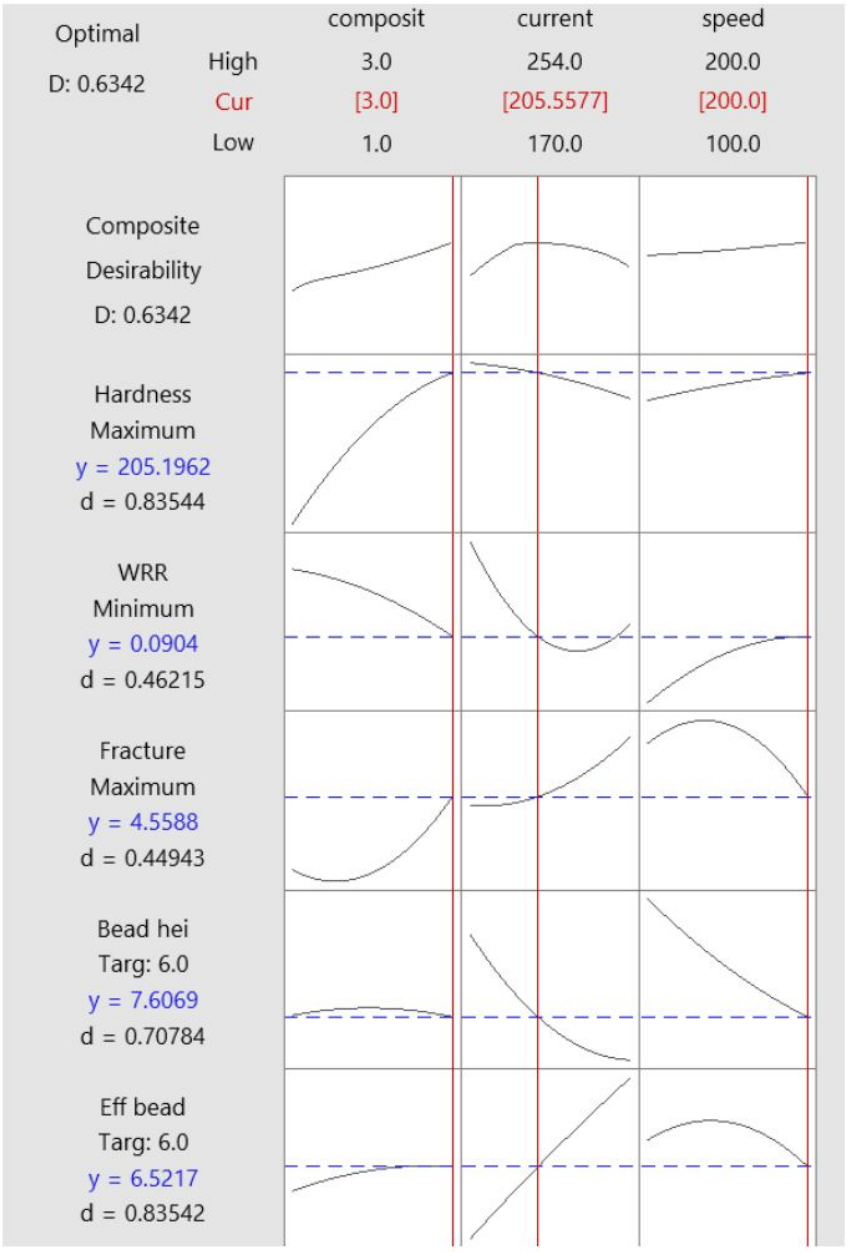

Fig. 5.15 optimal results with a composite desirability limit to address the multiple objective output response.

Chapter 6 Conclusions and Future Scope

6.1. Overview

This chapter concludes the work on different design strategies of functionally graded material (FGM) fabrication using WAAM-TIG process. The process parameter optimisation, feasibility study, Energy-dispersive X-ray spectroscopy, microstructure analysis, mechanical properties i.e., hardness and tribology properties such as COF and wear rate were performed on different FGM designs.

Further, Statistical optimization of process parameters composition, current and travel speed was performed to control mechanical, geometrical and tribological properties. CCD was used to design the parameters combination for response optimization.

6.2. Conclusion (Module 1)

- The presented experimental research showed the potential to fabricate the defect free SS316L+IN625 FGMs of continuous (CG-FGM) and sandwich (SW-FGM) type using dual wire WAAM-TIG process.
- A heuristic approach was employed to optimise the deposition parameters, where the deposition speed of 0.2 m/min and input current of 170 A was found suitable for the wfs range of 0.4–4 m/min.
- In the case of CG-FGM, quantitative EDS area scan analysis confirmed the Fe and Ni weight percent variation as per the design, whereas in the case of SW-FGM, the three designed peaks shifted downwards with Ni dominating the top.
- The performed elemental mapping confirmed the gradual transition of Fe and Ni at the interface.
- The microstructure in CG-FGM exhibited cellular to fine, and further to coarse columnar transition.
- SW-FGM showed a large layer interface region of ~300 μm due to subsequent heating and remelting of the previous layers while depositing a new layer.

- It was found that a minimum of two successive layers of deposition is recommended to achieve the distinct material regions.
- The hardness variation was found to exhibit linear increase and wavy pattern in CG-FGM and SW-FGM, respectively.
- XRD analysis showed that the formation of austenitic phase and variation in peak heights corelates to the change in microstructure and hardness.
- Linear reciprocating tribology test revealed that with the increase of Ni content in CG-FGM, specific wear rate is decreasing, and COF is increasing gradually.
- In SW-FGM, COF and wear rate showed strong dependency on adopted design.

6.3. Conclusion (Module 2)

- In factors effect on response analysis, the composition was found to be the main factor that effected the hardness, fracture toughness, scratch hardness, specific wear rate, and COF, while current and speed effected the bead geometry.
- In response surface design analysis, the models developed the regression equations for all responses with an R^2 value between 0.65 - 0.9%. The quadratic model was found best for majority of responses.
- In this study, hardness and fracture toughness were maximised and wear rate was minimised. The bead width and height were targeted with 6 mm each for accurate dimension of part to be manufactured.
- The optimum conditions obtained were composition of 3 (3:1), current of 205 A, and voltage of 200 mm/min.
- The predicted values of hardness, specific wear rate, fracture toughness, bead width and height are 205 HV, 0.0904 mm^3/mm, 4.56, 7.60 mm and6.52 mm respectively with composite desirability of 0.63.

6.4. Future Scope

- The experimental validation of the models with experimentally measured from the parameters obtained by targeting or maximizing or minimizing the responses.
- The fabrication and simulation of complete part using the developed models and further calculating the error of the complex part.
- The improvement of model's accuracy can be performed by neglecting the factors that are not contributing to the response.

REFERENCES

[1] Kawasaki A, Watanabe R. Thermal fracture behavior of metal/ceramic functionally graded materials. Eng Fract Mech. 2002;69:1713–1728.

[2] Meyers MA, McKittrick J, Chen PY. Structural biological materials: Critical mechanics-materials connections. Science (80-). 2013;339:773–779.

[3] Pareige P, Russell KF, Stoller RE, et al. Influence of long-term thermal aging on the microstructural evolution of nuclear reactor pressure vessel materials: An atom probe study. J Nucl Mater. 1997;250:176–183.

[4] Mohan Kumar S, Rajesh Kannan A, Pravin Kumar N, et al. Microstructural Features and Mechanical Integrity of Wire Arc Additive Manufactured SS321/Inconel 625 Functionally Gradient Material. J Mater Eng Perform. 2021;30:5692–5703. Available from: https://doi.org/10.1007/s11665-021-05617-3.

[5] Senthil TS, Ramesh Babu S, Puviyarasan M, et al. Mechanical and microstructural characterization of functionally graded Inconel 825 - SS316L fabricated using wire arc additive manufacturing. J Mater Res Technol [Internet]. 2021;15:661–669. Available from: https://doi.org/10.1016/j.jmrt.2021.08.060.

[6] Ghanavati R, Naffakh-Moosavy H. Additive manufacturing of functionally graded metallic materials: A review of experimental and numerical studies. J Mater Res Technol [Internet]. 2021;13:1628–1664. Available from: https://doi.org/10.1016/j.jmrt.2021.05.022.

[7] Chandrasekaran S, Hari S, Amirthalingam M. Functionally graded materials for marine risers by additive manufacturing for high-temperature applications: Experimental investigations. Structures. 2022;35:931–938.

[8] Torkamany MJ, Tahamtan S, Sabbaghzadeh J. Dissimilar welding of carbon steel to 5754 aluminum alloy by Nd:YAG pulsed laser. Mater Des. 2010;31:458–465.

[9] Nemat-Alla MM, Ata MH, Bayoumi MR, et al. Powder Metallurgical Fabrication and Microstructural Investigations of Aluminum/Steel Functionally Graded Material. Mater Sci Appl. 2011;02:1708–1718.

[10] Suryakumar S, Somashekara MA. Manufacturing of functionally gradient materials by using weld-deposition. 2013;505–508.

[11] El-Galy IM, Saleh BI, Ahmed MH. Functionally graded materials classifications and development trends from industrial point of view. SN Appl Sci. 2019;1.

[12] Maschinenbau VDF, Energiesysteme E-. Tool Path Planning for Wire-Arc Additive Manufacturing Processes. 2022;

[13] Zhang X, Chen Y, Liou F. Fabrication of SS316L-IN625 functionally graded materials by powder-fed directed energy deposition. Sci Technol Weld Join [Internet]. 2019;24:504–516. Available from: https://doi.org/10.1080/13621718.2019.1589086.

[14] Jafari D, Vaneker THJ, Gibson I. Wire and arc additive manufacturing : Opportunities and challenges to control the quality and accuracy of manufactured parts. Mater Des [Internet]. 2021;202:109471. Available from: https://doi.org/10.1016/j.matdes.2021.109471.

[15] Haidiezul AHM, Hazwan MHM, Soon Lee W, et al. Full Factorial Design Exploration Approach for Multi-Objective Optimization on the (FDM) 3D Printed Part. IOP Conf Ser Mater Sci Eng. 2020;917.

[16] Yang B, Lai Y, Yue X, et al. Parametric Optimization of Laser Additive Manufacturing of Inconel 625 Using Taguchi Method and Grey Relational Analysis. Scanning. 2020;2020.

[17] Kechagias JD, Vidakis N. Parametric optimization of material extrusion 3D printing process: an assessment of Box-Behnken vs. full-factorial experimental approach. Int J Adv Manuf Technol [Internet]. 2022;121:3163–3172. Available from: https://doi.org/10.1007/s00170-022-09532-2.

[18] Salih RM, Kadauw A, Zeidler H, et al. Investigation of LCD 3D Printing of Carbon Fiber Composites by Utilising Central Composite Design. J Manuf Mater Process. 2023;7:58.

[19] Carroll BE, Otis RA, Borgonia JP, et al. Functionally graded material of 304L stainless steel and inconel 625 fabricated by directed energy deposition: Characterization and thermodynamic modeling. Acta Mater [Internet]. 2016;108:46–54. Available from: http://dx.doi.org/10.1016/j.actamat.2016.02.019.

[20] Meng W, Zhang W, Zhang W, et al. Additive fabrication of 316L/Inconel625/Ti6Al4V functionally graded materials by laser synchronous preheating. Int J Adv Manuf Technol. 2019;104:2525–2538.

[21] Rodrigues TA, Bairrão N, Farias FWC, et al. Steel-copper functionally graded material produced by twin-wire and arc additive

manufacturing (T-WAAM). Mater Des [Internet]. 2022;213:110270. Available from: https://doi.org/10.1016/j.matdes.2021.110270.

[22] Mohan Kumar S, Rajesh Kannan A, Pravin Kumar N, et al. Microstructural Features and Mechanical Integrity of Wire Arc Additive Manufactured SS321/Inconel 625 Functionally Gradient Material. J Mater Eng Perform. 2021;30:5692–5703.

[23] Bobbio LD, Bocklund B. Experimental analysis and thermodynamic calculations of an additively manufactured functionally graded material of V to Invar 36. 2018;1–8.

[24] Cunningham CR, Flynn JM, Shokrani A, et al. Invited review article: Strategies and processes for high quality wire arc additive manufacturing. Addit. Manuf. 2018. p. 672–686.

[25] Ituarte IF, Boddeti N, Hassani V, et al. Design and additive manufacture of functionally graded structures based on digital materials. Addit Manuf. 2019;30.

[26] Singh J, Kumar M, Sharma A, et al. We are IntechOpen , the world ' s leading publisher of Open Access books Built by scientists , for scientists TOP 1 %. Intech [Internet]. 2016;11:13. Available from: https://www.intechopen.com/books/advanced-biometric-technologies/liveness-detection-in-biometrics.

[27] Khademzadeh S, Gennari C, Zanovello A, et al. Development of Micro Laser Powder Bed Fusion for Additive Manufacturing of Inconel 718. Materials (Basel). 2022;15.

[28] Imanian ME, Biglari FR. Modeling and prediction of surface roughness and dimensional accuracy in SLS 3D printing of PVA/CB composite using the central composite design. J Manuf Process [Internet]. 2022;75:154–169. Available from: https://doi.org/10.1016/j.jmapro.2021.12.065.

[29] Hosseinzadeh M, Ghoreishi M, Narooei K. 4D printing of shape memory polylactic acid beams: An experimental investigation into FDM additive manufacturing process parameters, mathematical modeling, and optimization. J Manuf Process [Internet]. 2023;85:774–782. Available from: https://doi.org/10.1016/j.jmapro.2022.12.006.

[30] Lu C, Shi J. Relative density and surface roughness prediction for Inconel 718 by selective laser melting: central composite design and multi-objective optimization. Int J Adv Manuf Technol [Internet]. 2022;119:3931–3949. Available from: https://doi.org/10.1007/s00170-021-08388-2.

[31] Zhang Z, Shen J, Hu S, et al. Optimization of CMT Characteristic Parameters for Swing Arc Additive Manufacturing of AZ91 Magnesium Alloy Based on Process Stability Analysis. Materials (Basel). 2023;16.

[32] Raj Mohan R, Venkatraman R, Raghuraman S, et al. Influence of Planetary Ball Mill Parameters on Powder Flowability of AlSi10Mg with Niobium Carbide Using Central Composite Design (CCD). Adv Mater Sci Eng. 2022;2022.

[33] El-Sayed MA, Essa K, Ghazy M, et al. Design optimization of additively manufactured titanium lattice structures for biomedical implants. Int J Adv Manuf Technol. 2020;110:2257–2268.

[34] Ghelich R, Jahannama MR, Abdizadeh H, et al. Central composite design (CCD)-Response surface methodology (RSM) of effective electrospinning parameters on PVP-B-Hf hybrid nanofibrous composites for synthesis of HfB 2 -based composite nanofibers. Compos Part B Eng. 2019;166:527–541.

[35] Khan AU, Madhukar YK. Effects of Pillar-Based Substrate on the Wire Arc Additive Manufacturing Process. Int J Precis Eng Manuf [Internet]. 2021;22:1311–1321. Available from: https://doi.org/10.1007/s12541-021-00529-7.

[36] Singh A, Negi S, Kapil S, et al. A comprehensive study of auxiliary arrangements for attaining omnidirectionality in additive manufacturing machine tools. J Manuf Sci Eng Trans ASME. 2021;143.

[37] Liu J, To AC. Quantitative texture prediction of epitaxial columnar grains in additive manufacturing using selective laser melting. Addit Manuf. 2017;16:58–64.

[38] Liu DR, Wang S, Yan W. Grain structure evolution in transition-mode melting in direct energy deposition. Mater Des. 2020;194.

[39] Theriault A, Xue L, Dryden JR. Fatigue behavior of laser consolidated IN-625 at room and elevated temperatures. Mater Sci Eng A. 2009;516:217–225.

[40] Lin X, Yue TM. Phase formation and microstructure evolution in laser rapid forming of graded SS316L / Rene88DT alloy. 2005;402:294–306.

[41] Elmer JW, Allen SM, Eagar TW. Microstructural Development during Solidification of Stainless Steel Alloys. 1989;

[42] Pinomaa T, Lindroos M, Walbrühl M, et al. Acta Materialia The

significance of spatial length scales and solute segregation in strengthening rapid solidification microstructures of 316L stainless steel. Acta Mater [Internet]. 2020;184:1–16. Available from: https://doi.org/10.1016/j.actamat.2019.10.044.

[43] Krakow R, Johnstone DN, Eggeman AS, et al. Acta Materialia On the crystallography and composition of topologically close-packed phases in ATI 718Plus ®. 2017;130:271–280.

[44] Hoon S, Choi J, Eom Y, et al. A phenomenological study of a Sn – Ag – Al composite solder reinforced with Mg – MWCNT : Improved electrical conductivity and thermo-physical performance. Mater Des [Internet]. 2018;140:196–208. Available from: https://doi.org/10.1016/j.matdes.2017.11.073.

[45] Hoon S, Nam K, Kim Y, et al. Fabrication of pre-alloyed Al – Li powders with high Li content via thermal dehydrogenation of LiH and rapid solidi fi cation process. JMADE [Internet]. 2016;94:159–165. Available from: http://dx.doi.org/10.1016/j.matdes.2016.01.009.

[46] Yan X, Gao S, Chang C, et al. Effect of building directions on the surface roughness , microstructure , and tribological properties of selective laser melted Inconel 625. J Mater Process Tech [Internet]. 2021;288:116878. Available from: https://doi.org/10.1016/j.jmatprotec.2020.116878.

[47] Gault B, Raabe D, Chauvet E, et al. Acta Materialia Hot cracking mechanism affecting a non-weldable Ni-based superalloy produced by selective electron Beam Melting. 2018;142:82–94.

[48] Komarasamy M, Shukla S, Williams S, et al. Microstructure , fatigue , and impact toughness properties of additively manufactured nickel alloy 718. Addit Manuf [Internet]. 2019;28:661–675. Available from: https://doi.org/10.1016/j.addma.2019.06.009.

[49] Dinda GP, Dasgupta AK, Mazumder J. Laser aided direct metal deposition of Inconel 625 superalloy : Microstructural evolution and thermal stability. 2009;509:98–104.

[50] Murr LE, Martinez E, Gaytan SM, et al. and Mechanical Properties for a Nickel-Base Superalloy Fabricated by Electron Beam Melting. 2011;42:3491–3508.

[51] Hoon S, Lee H, Mo S, et al. Selective compositional range exclusion via directed energy deposition to produce a defect-free Inconel 718 / SS 316L functionally graded material. Addit Manuf [Internet]. 2021;47:102288. Available from: https://doi.org/10.1016/j.addma.2021.102288.

[52] Valério A, Morelhão SL. Usage of Scherrer's formula in X-ray diffraction analysis of size distribution in systems of monocrystalline nanoparticles. 2019;1–9. Available from: http://arxiv.org/abs/1911.00701.

[53] Zhang X, Chen Y, Liou F. Fabrication of SS316L-IN625 functionally graded materials by powder-fed directed energy deposition. Sci Technol Weld Join [Internet]. 2019;24:504–516. Available from: https://doi.org/10.1080/13621718.2019.1589086.

[54] Mariani FE, Ribeiro KSB, Lombardi AN, et al. Effect of Laser Polishing Post-Processing Technique on the Roughness and Wear Resistance of Inconel 625 Deposited by Laser Cladding on AISI 304L Stainless Steel. J Mater Eng Perform. 2021;30:6713–6721.

[55] Zhang DK, Ge SR, Qiang YH. Research on the fatigue and fracture behavior due to the fretting wear of steel wire in hoisting rope. Wear. 2003;255:1233–1237.

[56] Bose K, Wood RJK. Optimum tests conditions for attaining uniform rolling abrasion in ball cratering tests on hard coatings. Wear. 2005;258:322–332.

[57] Liang X, Wu D, Li Q, et al. Laser rapid manufacturing of stainless steel 316L/Inconel718 functionally graded materials: Microstructure evolution and mechanical properties. Int J Opt. 2010;2010:1–5.

[58] Chen B, Su Y, Xie Z, et al. Development and characterization of 316L / Inconel625 functionally graded material fabricated by laser direct metal deposition. 2020;123.

[59] Duraisamy R, Kumar SM, Kannan AR, et al. Tribological performance of wire arc additive manufactured 347 austenitic stainless steel under unlubricated conditions at elevated temperatures. J Manuf Process [Internet]. 2020;56:306–321. Available from: https://doi.org/10.1016/j.jmapro.2020.04.073.

[60] Kim JS, Kim IJ, Kim YG. Optimization of weld pitch on overlay welding using mathematical method. Int J Precis Eng Manuf. 2014;15:1117–1124.

[61] Akono AT, Randall NX, Ulm FJ. Experimental determination of the fracture toughness via microscratch tests: Application to polymers, ceramics, and metals. J Mater Res. 2012;27:485–493.